Two-component phase scintillation spectra in the auroral region: Observations and Model

Abdelhaq M Hamza[1], Kaili Song[1], Karim Meziane[1], and Jayachandran P. Thayyil[1]

[1]University of New Brunswick

August 22, 2023

Abstract

The random amplitude and phase fluctuations observed in trans-ionospheric radio signals are caused by the presence of electron density irregularities in the ionosphere. Ground-based measurements of radio wave signals provide information about the medium through which these signals propagate. The Canadian High Arctic Ionospheric Network (CHAIN) Global Position System (GPS) receivers record radio signals emitted by the GPS satellites, enabling the study of their spectral characteristics.This study presents examples of phase spectra with two power-law components. These components exhibit steeper spectral slopes at higher frequencies and shallower ones at lower frequencies. In most cases, the breaking frequency point is statistically larger than the frequency associated with the Fresnel scale under the Taylor hypothesis. To be more specific, we conducted a spectral characterization of sixty (60) events recorded by the CHAIN Churchill GPS receiver, which is located in the auroral oval. When fluctuations above the background level are only observed in the phase, the spectra tend to be systematically steeper. Conversely, the power increase in higher frequency fluctuations accompanying amplitude scintillation tends to result in shallower spectra. A basic yet powerful model of radio wave propagation through a turbulent ionosphere, characterized by a power law electron density spectrum, can help to explain the two power laws observed in the scintillation events presented in this study by identifying the role played by small-scale ionospheric irregularities in diffraction.

Two-component phase scintillation spectra in the auroral region: Observations and Model

Hamza, A. M., K. Song, K. Meziane, P. T. Jayachandran

Physics Department, University of New Brunswick, Fredericton, New Brunswick, Canada

Key Points:

- Dual power-law spectra observed in phase scintillation in the auroral region.
- Refraction versus diffraction.
- Ionospheric irregularities and their connection to amplitude and phase scintillation.

Abstract

The random amplitude and phase fluctuations observed in trans-ionospheric radio signals are caused by the presence of electron density irregularities in the ionosphere. Ground-based measurements of radio wave signals provide information about the medium through which these signals propagate. The Canadian High Arctic Ionospheric Network (CHAIN) Global Position System (GPS) receivers record radio signals emitted by the GPS satellites, enabling the study of their spectral characteristics.This study presents examples of phase spectra with two power-law components. These components exhibit steeper spectral slopes at higher frequencies and shallower ones at lower frequencies. In most cases, the breaking frequency point is statistically larger than the frequency associated with the Fresnel scale under the Taylor hypothesis. To be more specific, we conducted a spectral characterization of sixty (60) events recorded by the CHAIN Churchill GPS receiver, which is located in the auroral oval. When fluctuations above the background level are only observed in the phase, the spectra tend to be systematically steeper. Conversely, the power increase in higher frequency fluctuations accompanying amplitude scintillation tends to result in shallower spectra. A basic yet powerful model of radio wave propagation through a turbulent ionosphere, characterized by a power law electron density spectrum, can help to explain the two power laws observed in the scintillation events presented in this study by identifying the role played by small-scale ionospheric irregularities in diffraction.

Plain Language Summary

This study discusses the impact electron density irregularities in the ionosphere have on radio wave propagation. Ground-based measurements of Global Navigation Satellite System (GNSS) signals provide insights into their spectral characteristics. The study presents examples of phase spectra with two power-law components, showing steeper slopes at higher frequencies and shallower ones at lower frequencies. Phase fluctuations tend to result in steeper spectra, while amplitude scintillations lead to shallower spectra. The study suggests a simple model of radio wave propagation through a turbulent ionosphere to explain these observations.

1 Introduction

Radio wave scintillation is a physical phenomenon, first discovered by radio astronomers (see Hey et al. 1947), and associated with the distortion of radio waves emitted by astronomical sources and propagating through conducting media. Ionospheric scintillation is a particular case of the more general phenomenon of radio scintillation attributed to the distortion of radio waves emitted by the Global Navigation Satellite System (GNSS) when propagating through a turbulent ionosphere (Kintner et al., 2007; Rino, 1979). The cause of these signal fluctuations is attributed to the presence of irregularities in the ionospheric electron density. These irregularities arise when free energy is available in the form of currents or large-scale pressure gradients to trigger instability mechanisms, such as the Farley-Buneman and Gradient-Drift instabilities, which in turn redistribute the energy in space and time (Aarons, 1997; Rino et al., 1981). The conventional theories suggest that when the linear threshold conditions are met the instabilities are triggered and waves will grow until quasi-linear and nonlinear effects will dissipate the currents and flatten the gradients to bring back the plasma to thermodynamic equilibrium. The return to equilibrium happens through the temporal and spatial redistribution of the free energy (see Francis F. Chen 2016), which in turn impose the observed power spectra.

Radio waves propagating through the structured ionosphere undergo scattering, and it is the characteristics of various scattering processes that allow us to extract some of the fundamental ionospheric properties. On the ground, ionospheric scintillations are observed using Global Positioning System (GPS) receivers, which record time series and display patterns that are largely determined by the spatial and temporal conditions of the ionospheric medium through which the radio signals propagate (Mezaoui et al., 2014; Jayachandran et al., 2017; Labelle & Kelley, 1986; Basu et al., 1990; Fremouw, 1980; Rufenach, 1972; Rino, 1979; Crane, 1976). The spectral analysis of scintillations is particularly valuable since it reveals some of the characteristics of these irregularities (Rino, 1979; Yeh & Liu, 1982; Wernik et al., 2003; Song et al., 2021). Many studies have been conducted to try and resolve the refractive effects from the diffractive ones (see McCaffrey and Jayachandran, 2019; Ghobadi et al., 2020; McCaffrey and Jayachandran, 2021; Conroy et al., 2022) without bringing the problem to a close. Part of the challenge is due to signal detrending, and many methods have been proposed in the literature (see Forte and Radicella, 2002; Mushini et al., 2012; Spogli et al., 2021). The lack of a basic physical model, which would clearly identify the refractive from the diffractive effects, needs to be remedied, and we propose to do so in the second part of this manuscript.

By analogy with fluid turbulence, in a turbulent three-dimensional (3D) plasma, the energy cascades, i.e. the redistribution of energy, from the large scales to the smaller scales (Haerendal, 1973). This cascade of energy leads to power law spectra that reflect the partitioning of power among the various scale lengths on time scales often dictated by the growth and decay of irregularities in the plasma. When a fluid is constrained to flow within horizontal planes with negligible horizontal divergence, it exhibits 2D behaviour. A key feature of two-dimensional turbulence is the preferential accumulation of energy at large scales, where the energy inverse-cascades from smaller to larger scales. However, the dissipation of enstrophy occurs at small scales, leading to an inertial spectral range where enstrophy is transferred from large to small scales (Chen, 2006).

Plasma density irregularities ranging from scales of 100 km to few meters (the ion gyroradius) are observed in the high latitude ionosphere (Aarons, 1997; Rino et al., 1981). Notably, Jin et al. (2019) conducted recent research that uncovered double slope power spectra in electron density, with clearly defined breaking scales spanning from 33 m to 330 m. The transition to a steeper power-law would occur at scale size irregularities shorter than 125 m (Basu et al., 1990). Additionally, Spicher et al. (2014) reported that the electron density measured by the ICI-2 sounding rocket in the high-latitude ionospheric F layer plasma exhibits double-slope power laws in regions of strong density gradients, which can be associated with polar cap enhanced density regions and their front or trailing edges in particular. These findings establish connections between the existing body of experimental evidence of fluid-like plasma turbulence in the ionosphere and the predictions of various fluid plasma models proposed to describe the dynamics of the turbulent ionosphere.

In the present work, we take advantage of the large body of literature about two-dimensional (2D) Navier-Stokes turbulence (Leith, 1971) to try and understand the signatures observed in the GNSS data by constructing a simple wave propagation model. The physical mechanisms leading to the dual-cascade of enstrophy and energy observed in two-dimensional fluid turbulence can help us understand the signatures in the radio signals recorded by ground-based GPS receivers at auroral latitudes. In section 2, we describe the data collection. In section 3, the data analysis is conducted and the results are presented. Finally, section 4 is dedicated to a simple wave-propagation model to explain the results of the analysis and shed some light on the power-laws observed.

2 Data Description

The Canadian High Arctic Ionospheric Network (CHAIN) is a distributed array of ground-based radio instruments located in the Canadian Arctic region. CHAIN is designed to take advantage of Canadian geographic vantage points for monitoring and studying the high latitude ionosphere (Jayachandran et al., 2009). CHAIN instruments are GNSS Ionospheric Scintillation and TEC Monitors (GISTM) and High Frequency (HF)

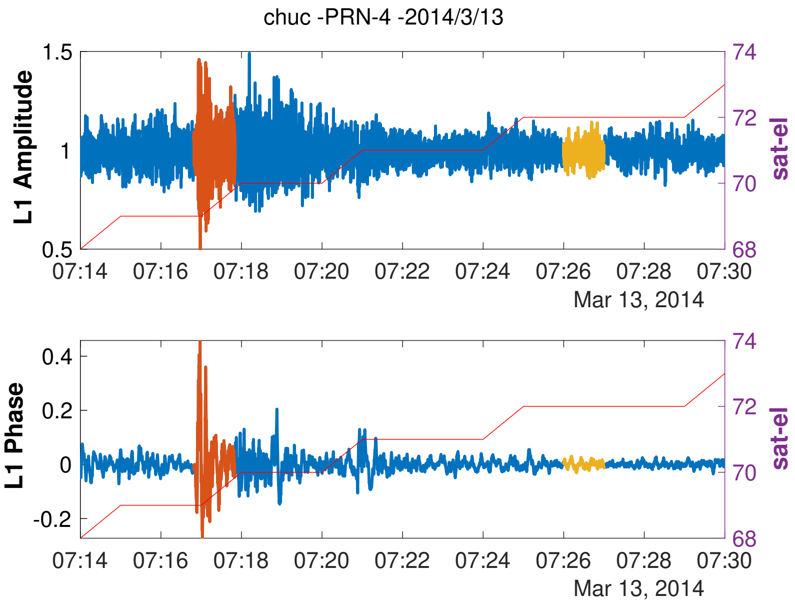

Figure 1. GPS L1 (1.575 GHz) measurements from 0714 to 0730 UTC for PRN4 at Churchill station (*chuc*) on Mar 13, 2014. While the top panel shows the signal amplitude, the bottom panel reports the carrier phase.

radars. The GISTMs in operation are Novatel GSV4004B and Septentrio PolaRxS Pro GNSS receivers (Van Dierendonck et al., 1993; Bougard et al., 2011). The Septentrio PolaRxS Pro is a multi-frequency, multi-constellation receiver, racking the L1, L2 and L5 signals independently of each other, and is designed for ionospheric studies and space weather applications. Each CHAIN receiver collects GPS observables from all visible GPS satellites. CHAIN has few locations with GISTM receivers recording data on L1, L2, and L5 frequencies at a 100 Hz sampling rate. For the present study, measurements collected at the Churchill (*chuc*) station (Geographic latitude 58.76 N, Geographic longitude 265.91E) provide data at 100 Hz sampling rate.

3 Results

For the present study, sixty-one scintillation events at the Churchill stations have been identified and selected during the time interval ranging from the year 2014 to 2021. A standard sixth-order Butterworth filter with a cutoff frequency of $f_c = 0.1$ Hz was used to detrend the amplitude and phase fluctuations. After obtaining the detrended signals, the amplitude and phase indices S_4 and σ_Φ are computed and used to identify scintillation events in the amplitude and phase, respectively. All scintillation events used in this analysis with scintillation indices S_4 and σ_ϕ are less than 0.1, which can be attributed to a weak scintillation regime. Once an event is selected, the spectral analysis of phase variations is carried out.

Figure 1 illustrates an example of phase and amplitude measurements collected at the *chuc* station for GPS PRN4, taken at a high elevation angle on March 13, 2014, from 0714 UT to 0730 UT. The top and bottom panels depict the detrended amplitude and phase at the L1 frequency, respectively. The right y-axis indicates the elevation angle in degrees. Our focus is on the time interval between 07:18:00 and 07:19:10 UT, highlighted by the red traces. During this interval (red trace), Figure 1 illustrates variations

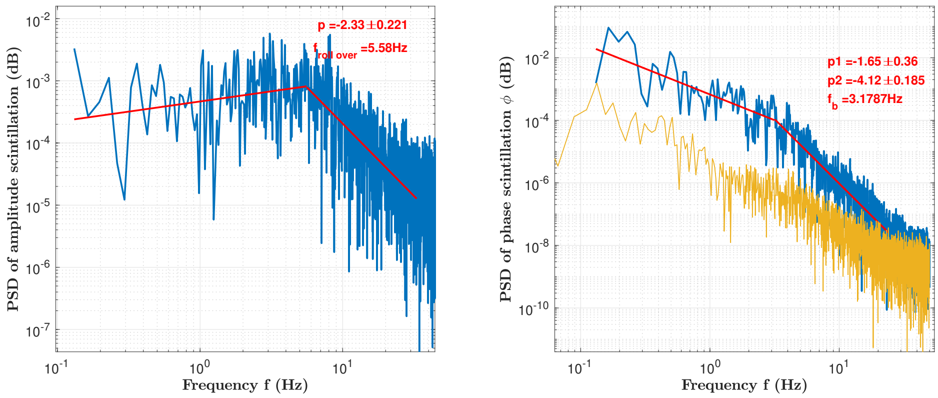

Figure 2. Left panel: amplitude scintillation spectrum. Right panel: Phase scintillation spectrum (blue) and the background noise spectrum is shown in yellow. On both panels, the best linear fit to fluctuations is indicated by the red straight line.

in carrier phase while observing minimal fluctuations in amplitude. Throughout the entire period of interest, both the signal amplitude and phase consistently remain elevated above the background level (yellow trace). We now proceed with the analysis by examining the spectral characteristics of the observed signal fluctuations. The spectral analysis of the phase and amplitude scintillation obtained for L1 is presented in Figure 2.

In Figure 2, the left panel provides the power density spectrum of amplitude scintillation. The right panel displays the phase scintillation spectrum (in blue) along with the background noise phase spectrum (in yellow). The red line represents the best fit for the measured spectrum. All spectra were obtained using the Fast Fourier Transform, with a time window of approximately 1 minute, and are presented in a log-log scale. Particularly, the amplitude scintillation spectrum exhibits a plateau below a critical frequency, denoted as f_0. This plateau suggests a region of relatively constant power density in the amplitude scintillation. The fit parameters for the amplitude spectrum include the spectral slope ($p = 2.33 \pm 0.22$) and the breaking frequency ($f_0 = 5.58$ Hz), which are labeled in the left panel of Figure 2. In contrast, the phase spectrum demonstrates two distinct components above the noise floor, in contrast to previously observed spectra with a single spectral slope. The noise spectrum (depicted in yellow) aids in visually identifying the noise frequency. A breakpoint frequency of $f_b = 3.9$ Hz is observed in the phase spectrum, indicating a transition between the two slopes. More precisely, the power density spectrum in Figure 2 reveals a distinct double-slope pattern for frequencies below approximately 11 Hz. Within this range, there are two distinct regions with different spectral slopes. The lower-frequency region, spanning from 0.1 Hz to 3.9 Hz, exhibits a relatively moderate slope of $p_1 = -1.79{\pm}0.245$. On the other hand, the higher-frequency region, ranging from 3.9 Hz to 11 Hz, displays a steeper slope of $p_1 = -4{\pm}0.236$. The precise values of the fit parameters and their corresponding errors are provided for each panel in Figure 2. The disparity in slope values between p_2 and p_1 is evident, indicating that the higher-frequency region exhibits a more pronounced and steeper change compared to the lower-frequency region. This finding is consistent with the study conducted by Spicher et al. (2014). Furthermore, when comparing the phase scintillation spectrum and the amplitude scintillation spectrum, clear differences can be observed. The amplitude scintillation spectrum displays a single slope above the critical frequency $f_0 = 5.58$ Hz, indicating a consistent spectral behavior. However, the phase scintillation spectrum exhibits a distinct double-slope pattern with a breakpoint frequency of $f_b = 3.9$ Hz. The

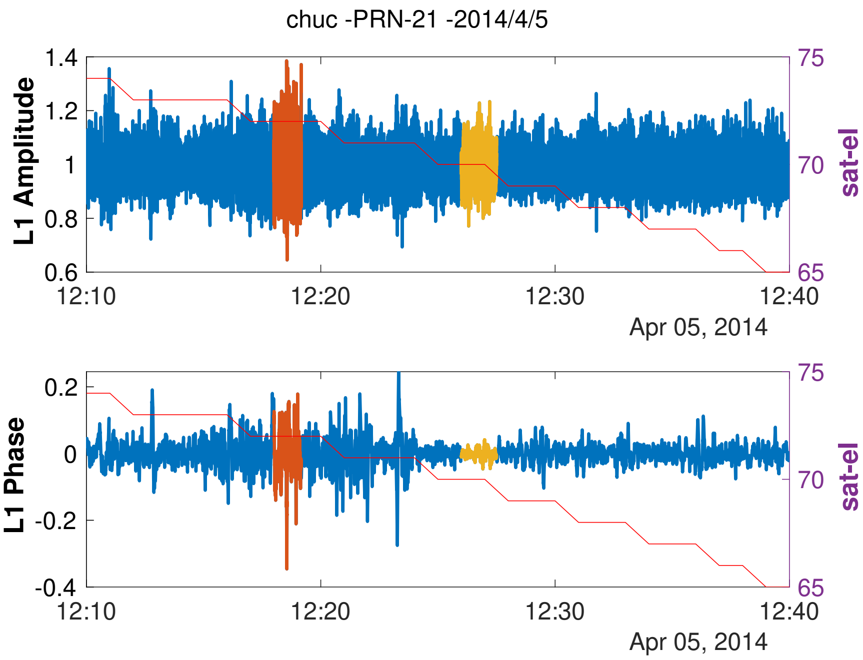

Figure 3. GPS L1 (1.575 GHz) measurements from 1210 to 1240 UTC for PRN21 at Churchill station (*chuc*) on April, 5, 2014. While the top panel shows the signal amplitude, the bottom panel depicts the carrier phase.

presence of two distinct components in the phase spectrum indicates that the spectral slopes differ from those observed in the amplitude spectrum. It is worth noting that the critical frequency f_0 in the amplitude scintillation spectrum is not equal to the break-point frequency f_b in the phase scintillation spectrum.

Figure 3 presents a second example that exhibits similar characteristics to the previously analyzed event. The top and bottom panels of Figure 3 display the recorded signal amplitude and phase measurements, respectively, obtained from the *chuc* station for GPS PRN21 at a high elevation angle on April 5, 2014, between 12:10 and 12:40 UT. During a specific time interval (12:18:30-12:19:30 UT), significant variations in both phase and amplitude were observed, indicating the onset of amplitude and phase scintillation (represented by the red trace). The yellow trace represents the background noise, which assists in determining the noise phase spectrum. Figure 4 illustrates the power density spectra of amplitude and phase scintillation obtained by applying the Fast Fourier Transform (FFT) to a 60-second time window. The left panel displays the amplitude scintillation spectrum, while the right panel shows the phase scintillation spectrum. In contrast to the amplitude spectrum, which exhibits a single slope characterized by $p = -2.26 \pm 0.17$, the phase spectrum demonstrates a double-slope profile. This indicates the presence of two distinct spectral ranges suggesting two different physical mechanisms at play. By performing linear fits, the slope values for each segment of the phase spectrum can be determined. The lower-frequency region, ranging from 0.1 Hz to 3.9 Hz, exhibits a relatively shallow slope of $p_1 = 1.79 \pm 0.245$, while the higher-frequency region, spanning from 3.9 Hz to 11 Hz, displays a steeper slope of $p_2 = 4 \pm 0.236$. Notably, the slope p_2 is found to be twice as big as p_1.

The same spectral analysis, as described above, was conducted for a total of sixty-one events collected between 2014 and 2021 at the *chuc* station. Figure 5 displays the

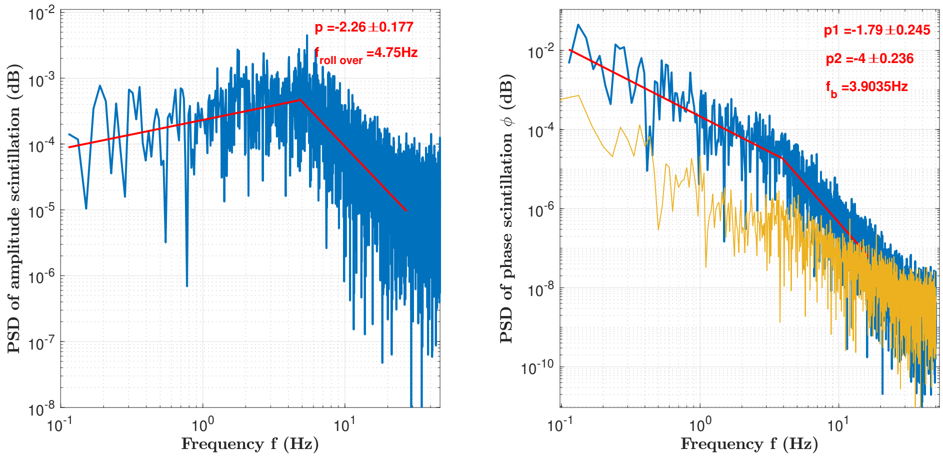

Figure 4. Same format as in Figure 2.

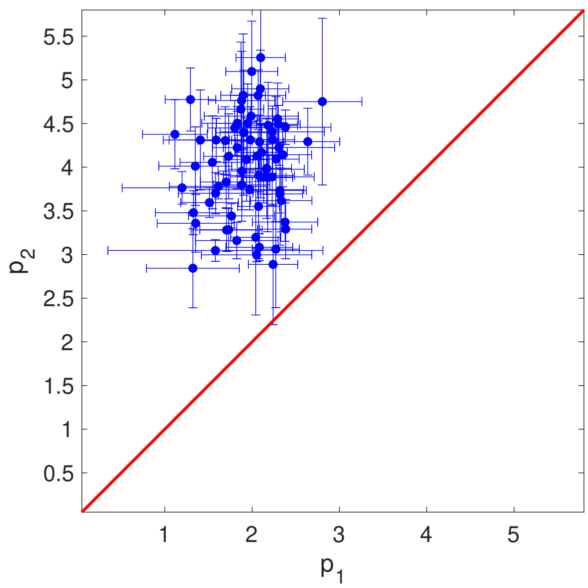

Figure 5. The p_2 values, representing the spectral power index of phase scintillation at higher frequencies (y-axis), are plotted against the corresponding p_1 values at lower frequencies (x-axis). The red straight line represents the line of slope unity.

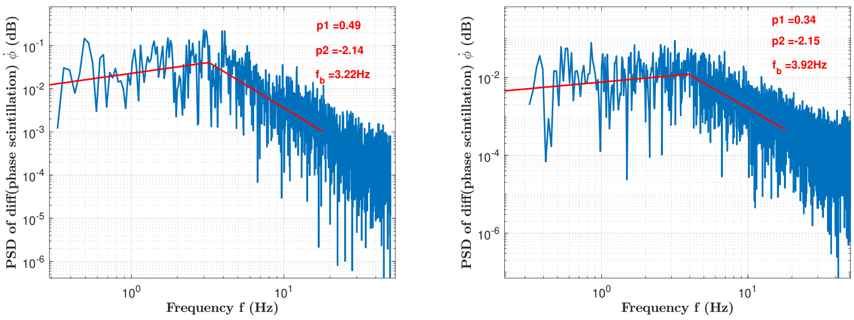

Figure 6.

results obtained from this analysis, comparing the spectral power index of phase scintillation at lower frequencies (y-axis) with the spectral power index at higher frequencies (x-axis). The error bars in the plot represent the uncertainty in the power index values, denoted by p. The red straight line in the plot represents the equality of spectral slope values between the two components of the phase scintillation spectral slopes p_1 and p_2. The results depicted in Figure 5 clearly demonstrate that, for all the scintillation events analyzed, the slope at higher frequencies is consistently steeper when compared to the slope at lower frequencies. This observation indicates that the high-frequency range of the phase scintillation spectrum exhibits a steeper spectral slope in comparison to the low-frequency portion.

In order to shed some light on the existence of two power-law spectra for the phase, we will compute the time-derivative of the phase and analyze its spectrum. When the Taylor hypothesis is satisfied, the time-derivative of the phase is directly related to the gradient of the phase, which represents the local component of the wave vector of the radio wave. if we denote by $\phi(\mathbf{x}, z, t)$ the phase of the propagating wave ($\mathbf{x} \equiv (x, y)$), the total time derivative of this phase is given by:

$$\frac{d\phi}{dt} = \frac{\partial \phi}{\partial t} + \mathbf{v}_d \cdot \nabla_{\perp} \phi + \frac{\partial \phi}{\partial z} \frac{\partial z}{\partial t}$$

where $\mathbf{v}_d$ represents a uniform drift velocity in the (x,y) plane (allowing the Taylor hypothesis to hold), and when we identify $\frac{\partial \phi}{\partial t} = -\omega$ and $\frac{\partial \phi}{\partial z} = k$ with the local frequency and the local z-component of the wave vector, k, we can clearly observe that the spectrum of the time-derivative of the phase depends very strongly on the gradient of the phase in the (x,y) plane as we shall demonstrate in section 4 below.

In the absence of small scale ionospheric electron density irregularities, the component of the phase-gradient along the direction of propagation is invariant and refraction is dominant. However, when small-scale electron density irregularities are present, diffraction takes over and large fluctuations in the phase-gradient along the direction of propagation arise as consequence. In other words, the time-derivative of the phase, when the Taylor hypothesis holds, represents this component of the phase-gradient, and its power spectrum should be directly related to the electron density power spectrum as will be discussed thoroughly in the section below describing an analytical model.

The phase derivative is obtained by differentiating the phase signal with respect to time and applying the Fourier Transform to obtain its spectrum. Figure 6 illustrates the phase derivative spectra for two scintillation events: the left panel corresponds to the event depicted in Figure 1, and the right panel corresponds to the event showcased in Figure 3. In Figure 6, it is clear that the phase derivative spectra display two distinct components with a breakpoint frequency, f_b, similar to the breakpoint frequency observed in Figure 2 and Figure 4, respectively. However, notable disparities in spectral slope values and overall shape are apparent when compared to the phase scintillation spectra depicted in the right panels of Figure 2 and Figure 4. Notably, the low-frequency region of the phase derivative spectrum appears flat, indicating minimal variations with a slope close to zero. Conversely, the high-frequency (corresponding to high wave numbers when the Taylor hypothesis holds) region of the spectrum aligns with the p_1 value observed in the right panels of Figure 2 and Figure 4, reflecting a steeper slope at small scales, large wave numbers. These findings provide valuable insights into the understanding of phase scintillation phenomena especially when it comes to separating the impacts of refraction from those of diffraction.

Table 1. Spectral slopes of derivative ($\dot{\phi}$ PSD) and Spectral slopes of phase scintillation (ϕ PSD)

Date of event	Spectral slope of $\dot{\phi}$ PSD		Spectral slope of ϕ PSD	
	p_1	p_2	p_1	p_2
2014/3/13	0.34	−2.1	−1.7	−3.9
2014/4/3	0.24	−1.8	−1.8	−3.3
2014/4/5	0.49	−2.1	−1.8	−4
2014/4/18	−0.08	−1.9	−2.1	−4.1
2014/4/20	0.10	−1.7	−1.8	−4.6
2014/4/28	0.20	−1.9	−1.7	−4.0
2014/10/26	−0.10	−2.0	−2.1	−4.0
2014/10/20	0.01	−1.7	−1.7	−4.7
2014/11/4	−0.09	−2.1	−2.1	−3.1
2018/9/10	0.11	−1.7	−1.6	−2.9
2017/9/8	−0.06	−1.8	−2.0	−3.8
2017/9/8	0.09	−1.7	−2.0	−3.2
2019/8/5	−0.02	−2.7	−2.6	−4.4
2021/5/12	−0.13	−2.2	−2.1	−3.6

Table 1 presents a summary of the double-spectral slopes for the phase derivative spectra and phase scintillation spectra. The first column of the table indicates the dates of the scintillation events. The second and third columns represent the spectral slopes, denoted as p_1, and p_2, respectively, in the phase derivative spectrum at the lower and higher frequency ranges. The fourth and fifth columns display the corresponding spectral slopes, p_1, and p_2, in the phase scintillation spectrum. It is clearly illustrated that the spectral slope of the phase derivative at lower frequencies tends towards zero. On the other hand, the spectral slope of the phase derivative at higher frequencies is similar to the spectral slope observed in the phase scintillation spectrum at lower frequencies. This observation suggests that the high-frequency portion of the phase derivative spectrum exhibits a slope comparable to the slope observed in the low-frequency portion of the phase scintillation spectrum.

4 A Radio Wave Propagation Model for the Dual Power Laws

Studies reported in the literature have suggested that Rayleigh-Taylor generated turbulence becomes anisotropic at intermediate and long wavelength (Bhattacharyya & Rastogi, 1986). Under such condition, there is no universal power law which describes the intermediate-scale irregularities(Franke et al., 1984).

As mentioned in Section 1, observational evidence for two-component irregularity power spectrum has been reported. Possible mechanisms giving rise to a break in the irregularity spectrum was discussed by (Bhattacharyya & Rastogi, 1986). It is evident that the presence of a break-point in the irregularity spectrum yields a two-component scintillation spectrum.

In our attempt to account for the two-component power law observed in the phase fluctuations, we have relied solely on the solution to the wave equation governing the propagation, which constitutes the backbone of the proposed model with no additional elements or hypothesis. From a fundamental point of view, the theoretical treatment of the propagation of an electromagnetic wave through a turbulent medium is a classical one, and might appear anachronistic given that it has attracted for many decades, and for various reasons, the interest of scientists and engineers.

In the ionospheric scintillation context, however, where refraction and diffraction are entangled, very few physical models are available to help underpin the pertinent factors that can fully capture the spectral features of the radio signal phase and amplitude fluctuations The simple model described below is an attempt to disentangle various scattering effects, and precisely addresses how the irregularity properties reflect on scintillation measurements on the ground. In particular, the model-framework presented in this section departs from some of the conventional standard formulation of scintillation models (Yu et al., 2018; Rino et al., 1981) by precisely identifying the role played by ionospheric irregularities in determining the type of scintillation event one should observe.

The fundamental equation describing the evolution of the electric and magnetic field components of an electromagnetic wave is given by:

$$\left\{\nabla^2 - \frac{\epsilon(\mathbf{x},z,t)}{c^2}\frac{\partial^2}{\partial t^2}\right\}\delta E_j(\mathbf{x},z,t) = 0 \tag{1}$$

where δE_j is any component of the electric field, $\epsilon(\mathbf{x},z,t)$ the medium dielectric function and c the speed of light in the vacuum. Further down the derivation, the j-index is omitted. The index of refraction is defined by:

$$n(\mathbf{x},z,t) = \sqrt{\epsilon(\mathbf{x},z,t)} \tag{2}$$

where ψ is the Fourier transform of $\delta E(\mathbf{x},z,t)$ in time, with

$$\delta E(\mathbf{x},z,t) = \frac{1}{2\pi}\int e^{i(kz-\omega t)}\psi(\mathbf{x},z,\omega)d\omega \tag{3}$$

Applying the Fourier transform to the wave equation (1) leads

$$2ik\frac{\partial\psi}{\partial z} + \nabla_\perp^2\psi + k^2(\epsilon-1)\psi = -\frac{\partial^2\psi}{\partial z^2} \tag{4}$$

given the definition of the dielectric function in its most simple form

$$\epsilon - 1 = n^2 - 1 = -\frac{4\pi e^2}{m\omega^2}N(\mathbf{x},z) \tag{5}$$

$$2ik\frac{\partial\psi}{\partial z} + \nabla_\perp^2\psi - r_e N(\mathbf{x},z)\psi = -\frac{\partial^2\psi}{\partial z^2} \tag{6}$$

where $r_e = \frac{4\pi e^2}{mc^2} \approx 2.8\times10^{-15}m$ is the classical electron radius.

We neglect the right hand side of the final equation (4) (The second order derivative with respect to the direction of propagation z). This approximation is often encountered in the literature as the "quasi-optics" approximation or "parabolic" approximation. The absence of a second derivative with respect the "z" means no curvature in the z-direction, which physically translates to the absence of reflected waves in the z-direction. The wave equation becomes:

$$2ik\frac{\partial\psi}{\partial z} + \nabla_{\perp}^{2}\psi - r_e N(\mathbf{x}, z)\psi = 0 \tag{7}$$

A note, worthy of mention, is the fact this last equation is the analog of the two-dimensional time-dependent Schrodinger equation, with time replaced by the spatial coordinate z, and the time dependent potential represented by the z-dependent electron density. There is a trivial invariant for the Schrodinger equation:

$$I = \int d\mathbf{x}|\psi(\mathbf{x}, z)|^2 = \int d\mathbf{x}|\psi(\mathbf{x}, 0)|^2 \tag{8}$$

The energy-like function $T(z)$ is not invariant.

$$T(z) = \int d\mathbf{x}\left[\frac{1}{2k}(\nabla_{\perp}\psi)^2 + \frac{r_e}{2k}N(\mathbf{x}, z)|\psi(\mathbf{x}, z)|^2\right] \tag{9}$$

with

$$\frac{dT(z)}{dz} = \frac{r_e}{2k}\int d\mathbf{x}\frac{\partial N(\mathbf{x}, z)}{\partial z}|\psi(\mathbf{x}, z)|^2 \tag{10}$$

The analog for energy $E(z)$ can be considered an adiabatic invariant when the dependence of the electron density on z is weak.

We now introduce the eikonal approximation and write $\psi(\mathbf{x}, z)$ as:

$$\psi(\mathbf{x}, z) = A(\mathbf{x}, z)\exp iS(\mathbf{x}, z) \tag{11}$$

where $A(\mathbf{x}, z)$ and $S(\mathbf{x}, z)$ are real functions. Note that we need to keep track of the fact that the total phase includes the term $e^{i(kz-\omega t)}$, which leads to a total phase $\phi(\mathbf{x}, z, t) = S(\mathbf{x}, z) + kz - \omega t$, and which suggests a slow z-dependence of $S(\mathbf{x}, z)$. We should point out the fact that the gradient and time derivative of the total phase define the local wave number and the local frequency as follows:

$$\begin{aligned}
\frac{\partial\phi}{\partial z} &= \frac{\partial S}{\partial z} + k \\
\nabla_{\perp}\phi &= \nabla_{\perp}S \\
\frac{\partial\phi}{\partial t} &= -\omega
\end{aligned} \tag{12}$$

We insert the expression for ψ (11) into the wave equation (7), which leads to a system of coupled equations describing the evolution of the amplitude and phase of the wave, respectively.

$$\frac{\partial S}{\partial z} - \frac{1}{2k}\frac{\nabla_{\perp}^{2}A}{A} + \frac{1}{2k}(\nabla_{\perp}S)^2 + \frac{r_e}{2k}N = 0 \tag{13}$$

$$\frac{\partial A^2}{\partial z} + \nabla_{\perp}\cdot[\frac{A^2}{k}\nabla_{\perp}S] = 0 \tag{14}$$

Note that if we neglect the variations of the amplitude in the plane perpendicular to the direction of propagation z, we obtain the following set of equations:

$$\frac{\partial S}{\partial z} + \frac{1}{2k}(\nabla_{\perp}S)^2 + \frac{r_e}{2k}N = 0 \tag{15}$$

$$\frac{\partial A^2}{\partial z} + \frac{A^2}{k}\nabla_{\perp}^{2}S = 0 \tag{16}$$

note that equation (16) can also be written in a more compact form as follows:

$$\frac{\partial \left[\ln A^2\right]}{\partial z} + \frac{1}{k}\nabla_\perp^2 S = 0 \tag{17}$$

Equations (15) shows the phase is directly affected by the electron density and its fluctuations. The second term in equation (15), $(\nabla_\perp S)^2$, is the refractive term. Indeed, one can define the local wave vector by its components $(\nabla_\perp S, k+\frac{\partial S}{\partial z})$, which suggests that the component $\nabla_\perp S$ determines the amount of rotation away from the z-axis when $\frac{\partial S}{\partial z}$ is negligible, and is therefore linked to refraction. On the other hand, equation (16) shows that the amplitude is affected by the curvature of the phase, $\nabla_\perp^2 S = \nabla_\perp \cdot \nabla_\perp S$, which is a measure of steepest descent and identifies minima and maxima in the wave fronts, and is directly linked to diffraction. Note also that this Laplacian can be interpreted in terms of the divergence of the local perpendicular component of the wave-vector $\nabla_\perp S$. In other words, in the absence of small scale structures in the electron density, the amplitude does not change (see (Song et al., 2023)). We should also point out the fact that refraction can be quantified by the ratio $\frac{|\nabla_\perp S|}{k}$, while diffraction depends solely of the curvature of the phase S.

The invariants (adiabatic invariant included), introduced above, can be expressed in terms of the amplitude and phase as follows,

$$\begin{aligned} I &= \int d\mathbf{x} A^2(\mathbf{x}, z) = \int d\mathbf{x} A^2(\mathbf{x}, 0) \\ T &= \frac{1}{2k}\int d\mathbf{x}\left[(\nabla_\perp A)^2 + (\nabla_\perp S)^2 A^2 + r_e N A^2\right] \end{aligned} \tag{18}$$

Since we are primarily interested in power spectra, we will use the two-dimensional Fourier transforms of the Amplitude and the phase as defined by:

$$\begin{aligned} A(\mathbf{x}, z) &= \int d\mathbf{q} e^{i\mathbf{q}\cdot\mathbf{x}} A(\mathbf{q}, z) \\ S(\mathbf{x}, z) &= \int d\mathbf{q} e^{i\mathbf{q}\cdot\mathbf{x}} S(\mathbf{q}, z) \end{aligned} \tag{19}$$

which in turn leads to the following equations for the Fourier components of the amplitude and phase, respectively,

$$\begin{aligned} S(\mathbf{q}, z) &= -\frac{r_e}{2k}\int^z dz_1 N(\mathbf{q}, z_1) \\ &+ \frac{k}{2}\int^z dz_1 \int d\mathbf{p}\frac{\mathbf{p}\cdot(\mathbf{q}-\mathbf{p})}{k^2} S(\mathbf{p}, z_1) S(\mathbf{q}-\mathbf{p}, z_1) \end{aligned} \tag{20}$$

$$\begin{aligned} \left[\ln A^2\right](\mathbf{q}, z) &= \frac{q^2}{k}\int^z dz_1 S(\mathbf{q}, z_1) \\ &+ k\int^z dz_1 \int d\mathbf{p}\frac{\mathbf{p}\cdot(\mathbf{q}-\mathbf{p})}{k^2} S(\mathbf{p}, z_1)\left[\ln A^2\right](\mathbf{q}-\mathbf{p}, z_1) \end{aligned} \tag{21}$$

Note that if we follow the notation in (Yeh & Liu, 1982) and write $A(\mathbf{x}, z) = e^{\chi(\mathbf{x}, z)}$, then $\left[\ln A^2\right] = 2\chi(\mathbf{x}, z)$. It becomes clear that the second equation (21) is nothing but the equation for the Fourier transform of $\chi(\mathbf{x}, z)$, which can be explicitly expressed as:

$$\chi(\mathbf{q}, z) = \frac{q^2}{2k}\int^z dz_1 S(\mathbf{q}, z_1) + k\int^z dz_1 \int d\mathbf{p}\frac{\mathbf{p}\cdot(\mathbf{q}-\mathbf{p})}{k^2} S(\mathbf{p}, z_1)\chi(\mathbf{q}-\mathbf{p}, z_1) \tag{22}$$

in fact, one can easily show the equation governing the variation of the amplitude with height (z) can be cast in the following form:

$$\frac{\partial \chi}{\partial z} + \nabla_\perp \chi \cdot \frac{\nabla_\perp S}{k} + \frac{1}{2k}\nabla_\perp^2 S = 0 \tag{23}$$

which, in the case when one can neglect the variation of the amplitude in the plane perpendicular to the direction of propagation or neglect the effects of refraction (second term in equation (23)), shows that the variation of the amplitude depends solely on the curvature of the phase. This clearly shows how diffraction affects the amplitude of the wave.

Note also that given the size of $r_e \approx 10^{-15}m$ and given the typical ionospheric densities of $N \approx 10^{11}m^{-3}$, the term $r_eN \approx 10^{-4}m^{-2}$.

From a dimensional analysis of equation (7), and introducing the Fresnel scale length $L_F = \sqrt{\lambda z} \approx 500$ m for the type of ionospheric problem we want to address, a perpendicular scale $L_\perp$ for the phase and a scale length L_c for the curvature of the phase, we can estimate from equations (15) and (16):

$$\left\{2k\frac{\partial S}{\partial z}\right\} \approx \frac{[S]}{L_F^2} \approx 4\times 10^{-6}[S] \quad ; \quad \left\{(\nabla_\perp S)^2\right\} \approx \frac{[S]^2}{L_\perp^2} \quad ; \quad \{r_eN\} \approx 10^{-4}m^{-2} \tag{24}$$

$$\left\{k\frac{\partial\left[\ln A^2\right]}{\partial z}\right\} \approx \frac{\left[\ln A^2\right]}{L_F^2} \approx 4\times 10^{-6}\left[\ln A^2\right] \quad ; \quad \left\{\nabla_\perp^2 S\right\} \approx \frac{[S]}{L_c^2} \tag{25}$$

comparing the size of these terms allows us to identify the dominant scattering mechanisms. In the absence of small scale structures in the density, and noting that the second term in equation (24) when dominant leads to the geometrical optics approximation and a mathematical description of refraction when balanced with the electron density term. On the other hand, when the electron density is structured and small scale structures arise with length scales comparable to the fresnel scale, diffraction kicks in, and the second term in equation (25) becomes large enough to affect the amplitude.

We will now focus on identifying the physical mechanism(s) responsible for the appearance of dominant power laws in the power spectrum for the phase of radio signals detected by GPS receivers located in the auroral zone. To accomplish this task, we turn to the invariants identified above and express them in terms of Fourier components of the amplitude and phase.

$$\begin{aligned}
I &= \int d\mathbf{x}|\psi(\mathbf{x},z)|^2 = \int d\mathbf{x}|A(\mathbf{x},z)|^2 \\
&= \int d\mathbf{q}|A(\mathbf{q},z)|^2 = \int d\mathbf{q}|A(\mathbf{q},z=0)|^2 \qquad (26)\\
2kT &= \int d\mathbf{q}q^2|A(\mathbf{q},z)|^2 \\
&+ r_e\int d\mathbf{q}N(\mathbf{q},z)\int d\mathbf{p}A(\mathbf{p},z)A^*(\mathbf{q}+\mathbf{p},z) \\
&+ \int d\mathbf{q}A(\mathbf{q},z)\int d\mathbf{p}\int d\mathbf{r}\left[\mathbf{r}\cdot(\mathbf{q}-\mathbf{p}-\mathbf{r})\right]A^*(\mathbf{p},z)S(\mathbf{r},z)S^*(\mathbf{q}-\mathbf{p}+\mathbf{r},z) \qquad (27)
\end{aligned}$$

Note that because $A(\mathbf{x},z)$ and $S(\mathbf{x},z)$ are real functions, the complex conjugates of their Fourier components satisfy $A^*(\mathbf{q},z) = A(-\mathbf{q},z)$ and $S^*(\mathbf{q},z) = S(-\mathbf{q},z)$. The first expression (26) is an absolute invariant while the second (27) is an adiabatic one as discussed above. Given the two expressions for the phase and the amplitude (20,21), there is clearly a closure problem. We shall iterate to only include terms to order r_e^2. The results are:

$$\begin{aligned}
I &= \int d\mathbf{q}|A(\mathbf{q},z=0)|^2 \qquad (28)\\
2kT &= \int d\mathbf{q}q^2|A(\mathbf{q},z)|^2 \\
&+ r_e\int d\mathbf{q}N(\mathbf{q},z)\int d\mathbf{p}A(\mathbf{p},z)A^*(\mathbf{q}+\mathbf{p},z) \\
&+ \frac{r_e^2}{4}\int d\mathbf{q}A(\mathbf{q},z)\int d\mathbf{p}\int d\mathbf{r}\left[\frac{\mathbf{r}\cdot(\mathbf{q}-\mathbf{p}-\mathbf{r})}{k^2}\right]A^*(\mathbf{p},z)\,*
\end{aligned}$$

$$* \quad \int^z dz_1 \int^z dz_2 N(\mathbf{r}, z_1) N(-\mathbf{q} + \mathbf{p} - \mathbf{r}, z_2) \tag{29}$$

We will now show that by imposing a single power law spectrum for the amplitude consistent with the first invariant, the second invariant will reveal two power laws, one directly related to the amplitude and a second one related to the electron density spectrum.

Let us assume that the amplitude and density spectra are isotropic and are given by:

$$\begin{aligned} |A(\mathbf{q}, z)|^2 &= C_A q^\alpha \quad for \quad q_{Ai} \le q \le q_{Ad} && (30) \\ |N(\mathbf{q}, z)|^2 &= C_N q^\beta \quad for \quad q_{Ni} \le q \le q_{Nd} && (31) \end{aligned}$$

where C_A, C_N are constants and where q_{Ai} and q_{Ad} are the limits of the amplitude spectrum. Similarly, q_{Ni} and q_{Nd} represent the limits of the electron density spectrum.

To order r_e, the two invariants are given by:

$$\begin{aligned} I &= 2\pi C_A \int_{q_{Ai}}^{q_{Ad}} dq q^{\alpha+1} && (32) \\ T &= \frac{\pi C_A}{k} \int_{q_{Ai}}^{q_{Ad}} dq q^{\alpha+3} \\ &+ \frac{r_e}{2k} \int d\mathbf{q} N(\mathbf{q}, z) \int d\mathbf{p} A(\mathbf{p}, z) A(-\mathbf{q} - \mathbf{p}, z) && (33) \end{aligned}$$

Given the assumption of isotropy, we can insert the expressions for the Fourier components of the amplitude and the density to obtain the power spectrum for the phase from the energy-like invariant T.

$$T = \frac{\pi C_A}{k} \int dq \left[q^{\alpha+3} + 2\pi r_e C_N^{\frac{1}{2}} q^{\frac{\beta}{2}+1} \left(\int^q + \int_q \right) dp |\mathbf{q} + \mathbf{p}]|^{\frac{\alpha}{2}} p^{\frac{\alpha}{2}+1} \right] \tag{34}$$

let us expand the $|\mathbf{q} + \mathbf{p}|^{\frac{\alpha}{2}} = (q^2 + p^2 + 2\mathbf{q} \cdot \mathbf{p})^{\frac{\alpha}{4}}$ as follows:

$$|\mathbf{q} + \mathbf{p}]|^{\frac{\alpha}{2}} = \begin{cases} q^{\frac{\alpha}{2}} \left(1 + \frac{p^2}{q^2} + 2\frac{\mathbf{q} \cdot \mathbf{p}}{q^2} \right)^{\frac{\alpha}{4}} & \text{if } q > p \\ p^{\frac{\alpha}{2}} \left(1 + \frac{q^2}{p^2} + 2\frac{\mathbf{q} \cdot \mathbf{p}}{p^2} \right)^{\frac{\alpha}{4}} & \text{if } p > q \end{cases}$$

which leads to the following expression for E when keeping the leading terms only:

$$T = \frac{\pi C_A}{k} \int dq \left[q^{\alpha+3} + 2\pi r_e C_N^{\frac{1}{2}} q^{\frac{\beta}{2}+1} \left(q^{\frac{\alpha}{2}} \int_{p_0}^q p^{\frac{\alpha}{2}+1} dp + \int_q^{p_1} p^{\alpha+1} dp \right) \right] \tag{35}$$

which finally leads to:

$$\begin{aligned} T &= \frac{\pi C_A}{k} \int dq \left[q^{\alpha+3} + 2\pi r_e C_N^{\frac{1}{2}} q^{\frac{\beta}{2}+1} \left(\frac{\alpha q^{\alpha+2}}{(\alpha+2)(\alpha+4)} - \frac{2q^{\frac{\alpha}{2}} p_0^{\frac{\alpha}{2}+2}}{\alpha+4} + \frac{p_1^{\alpha+2}}{\alpha+2} \right) \right] \\ &= \int dq \mathcal{E}(q) && (36) \end{aligned}$$

From this expression, we deduce the energy-like power spectrum:

$$\begin{aligned} \mathcal{E}(q) &= \frac{\pi C_A}{k} q^{\alpha+3} \\ &+ \frac{2\pi^2 r_e}{k} C_A C_N^{\frac{1}{2}} q^{\frac{\beta}{2}+\alpha+3} * \\ &* \left(\frac{\alpha}{(\alpha+2)(\alpha+4)} - \frac{2}{\alpha+4} \left(\frac{p_0}{q} \right)^{\frac{\alpha}{2}+2} + \frac{1}{\alpha+2} \left(\frac{p_1}{q} \right)^{\alpha+2} \right) && (37) \end{aligned}$$

Note that $(p_0/q) < 1$ and $(p_1/q) > 1$, and that for $-4 < \alpha < -2$ the last two terms in expression (37) can be dropped. This in turn leads to two dominant and competing terms in the energy-like power spectrum, and it is clear that for large q (small scales), the second term, which contains the information about the density spectrum, defines a new power law:

$$\mathcal{E}(q) \approx \frac{\pi C_A}{k} q^{\alpha+3} + \frac{2\pi^2 \alpha r_e C_A C_N^{\frac{1}{2}}}{k(\alpha+2)(\alpha+4)} q^{\frac{\beta}{2}+\alpha+3} \tag{38}$$

We now need to connect the phase power spectrum to the energy-like power spectrum $E(q)$. We can easily show and derive from equation (13) the following equation:

$$\int d\mathbf{x} A^2(\mathbf{x}, z) \frac{\partial S(\mathbf{x}, z)}{\partial z} + T(z) = 0 \tag{39}$$

the function $T(z)$ is by definition positive (see equation (18)), and consequently the first term should be negative for equation (39) to hold. We therefore conclude that the z-derivative of the phase should be small and negative; indeed, this is consistent with equation (15). We have assumed that $T(z) = T(0)$ is an adiabatic invariant, and this in turn allows us to deduce that the first term in equation (39) is also independent of z in the adiabatic limit. We should note that to first order in r_e the power spectrum of $\frac{\partial S(\mathbf{q},z)}{\partial z} = \dot{S}(\mathbf{q}, z)$ is the same as the power spectrum for the electron density (see equation (15)) when neglecting refraction (neglecting the term $(\nabla_\perp S)^2$ in equation (15)). However, when small scale structures arise in the density, one can no longer neglect the refractive term in equation (15) and the diffractive term in the amplitude equation (16), giving rise to competing power laws at two different scale ranges; a scale-range with scales much larger than the Fresnel scale, where diffractive effects are negligible, and a scale-range with small scales of the order of the Fresnel scale or smaller, where diffractive effects become dominant.

Since we are also interested in the power spectrum of $\frac{\partial S(\mathbf{q},z)}{\partial z} = \dot{S}(\mathbf{q}, z)$, equation (39) can be expressed in Fourier space.

$$\int d\mathbf{q} \dot{S}(\mathbf{q}, z) \int d\mathbf{p} A(\mathbf{p}, z) A(-(\mathbf{p}+\mathbf{q}), z) + \int dq \mathcal{E}(q) = 0 \tag{40}$$

note that we have already encountered the integral over $\mathbf{p}$ in equation (34). We can apply the same arguments to try and estimate this integral to obtain:

$$\int dq \left[-|\dot{S}(\mathbf{q}, z)| \frac{2\pi\alpha}{(\alpha+2)(\alpha+4)} + \frac{1}{2k} + \frac{\pi \alpha r_e C_N^{\frac{1}{2}}}{k(\alpha+2)(\alpha+4)} q^{\frac{\beta}{2}} \right] q^{\alpha+3} = 0 \tag{41}$$

if we assume the power spectrum of $\dot{S}(\mathbf{q}, z)$ to follow a power law, we can link the power index of the power spectrum for $\dot{S}$ to the power indices for the amplitude and the density. Note, as discussed above, that to first order in r_e the power spectrum for $\dot{S}$ is the power spectrum of the density as also suggested by the term in square brackets in equation (41).

$$\int dq \left[q^{\alpha+3} |\dot{S}(\mathbf{q}, z)| \right] = \frac{(\alpha+2)(\alpha+4)}{4\pi^2 C_A \alpha} T(z) = \frac{(\alpha+2)(\alpha+4)}{4\pi^2 C_A \alpha} T(0) \tag{42}$$

Equations (41) and (42) can be used interchangeably to calculate the power-law index of $\dot{S}$ in terms of the power-law indices for the amplitude and the density.

4.1 Summary: The Refractive limit

In the refractive limit, the curvature of the phase can be neglected and the equations governing the evolution of the amplitude and the phase of the propagating radio wave reduce to:

$$\frac{\partial \chi}{\partial z} + \left(\frac{\nabla_\perp S}{k} \right) \cdot \nabla_\perp \chi \quad \approx \quad 0$$

$$\frac{\partial S}{\partial z} + \frac{k}{2}\left(\frac{\nabla_\perp S}{k}\right)^2 + \frac{r_e}{2k}N \quad = \quad 0 \tag{43}$$

The ray-path is defined by

$$\frac{d\mathbf{x}}{dz} = \frac{\nabla_\perp S}{k}$$

which in turn leads to writing the equation for the amplitude as:

$$\frac{\partial \chi}{\partial z}dz + \nabla_\perp \chi \cdot d\mathbf{x} = d\chi \approx 0$$

which means that the amplitude does not change and the amplitude spectrum is invariant, which is consistent with the invariant analysis discussed above. The equation for the phase suggests that for small-angle refraction the phase is determined by the total electron content, which in this case is dominated by large scale electron density structures (small wave numbers). The refractive term in the equation for the phase (43) is quadratic and can be neglected for small-angle refraction, which leaves a phase completely dependent on the total electron content, and therefore a phase spectrum with very little power at large wave numbers.

4.2 Summary: The Diffractive Limit

In the diffractive limit, the gradient of the phase terms are neglected and the following set of governing equations is obtained:

$$\begin{aligned} \frac{\partial \chi}{\partial z} + \frac{1}{2k}\nabla_\perp^2 S \quad &\approx \quad 0 \\ \frac{\partial S}{\partial z} + \frac{r_e}{2k}N \quad &\approx \quad 0 \end{aligned} \tag{44}$$

This set of equations can also be written in the following form:

$$S(\mathbf{x}, z) \quad \approx \quad -\frac{r_e}{2k}\int^z N(\mathbf{x}, z_1)dz_1 \tag{45}$$

$$\begin{aligned} S(\mathbf{q}, z) \quad &\approx \quad -\frac{r_e}{2k}\int^z N(\mathbf{q}, z_1)dz_1 \\ \frac{\partial^2 \chi(\mathbf{x}, z)}{\partial z^2} \quad &\approx \quad \frac{r_e}{4k^2}\nabla_\perp^2 N(\mathbf{x}, z) \\ \chi(\mathbf{x}, z) \quad &\approx \quad \frac{r_e}{4k^2}\nabla_\perp^2 \int^z dz_1 \int^{z_1} N(\mathbf{x}, z_2)dz_2 \\ \chi(\mathbf{q}, z) \quad &\approx \quad -\frac{r_e}{4k^2}q^2 \int^z dz_1 \int^{z_1} N(\mathbf{q}, z_2)dz_2 \end{aligned} \tag{46}$$

equations (45) and (46) show explicitly how the phase and amplitude are related to the density and the total electron content, respectively, and how the power spectra at large wave numbers, when small scale density structures are present, are related to the density spectrum.

5 Discussion and Conclusion

The model presented above is a simple model yet powerful enough to predict spectra with two power-laws. It also sheds some light on the method to adopt to resolve the difference between refractive and diffractive effects. Equations (15) and (16) constitute the backbone of the model with terms easily identifiable with refraction, $(\nabla_\perp S)^2$, with diffraction, $\nabla_\perp^2 S$, and with the electron density N and therefore with the total electron content when integration over z is performed. When small scale density irregularities are absent and refraction is dominant, the amplitude remains invariant throughout propagation and the amplitude power-law spectrum is also invariant. However, when small scale irregularities are present, the curvature of the phase is no longer negligible, and the contribution of the diffractive term to the amplitude equation suggest a readjustment of the power law. Moreover, the invariant I (related to the Born rule in quantum mechanics) suggests a shallower amplitude power law, which reflects the redistribution of power to small scale, large q. On the other hand, the presence of small scales in the density leads to a phase power spectrum similar to the density power spectrum.

6 Open Research

Data Availability Statement CHAIN data are available through `http://www.chain-project.net/data/gps/data/raw/`

7 Acknowledgements

Infrastructure funding for CHAIN was provided by the Canada Foundation for Innovation (CFI) and the New Brunswick Innovation Foundation (NBIF). CHAIN is maintained in collaboration with the Canadian Space Agency (CSA). This research was undertaken with the financial support of the Canadian Space Agency FAST program and the Natural Sciences and Engineering Research Council of Canada. Part of the funding for this research is provided by the Natural Sciences and Engineering Research Council Canada (NSERC).

References

Aarons, J. (1997, August). Global positioning system phase fluctuations at auroral latitudes. *Journal of Geophysical Research: Space Physics*, *102*, 17219–17231. doi: 10.1029/97JA01118

Basu, S., Basu, S., MacKenzie, E., Coley, W. R., Sharber, J. R., & Hoegy, W. R. (1990). Plasma structuring by the gradient drift instability at high latitudes and comparison with velocity shear driven processes. *Journal of Geophysical Research: Space Physics*, *95*, 7799–7818. doi: 10.1029/JA095iA06p07799

Bhattacharyya, A., & Rastogi, R. G. (1986). Phase scintillations due to equatorial F region irregularities with two-component power law spectrum. *Journal of Geophysical Research*, *91*(A10).

Bougard, B., Sleewaegen, J. M., Spogli, L., & Sreeja, J. F., V. V. Galera Monico. (2011). Cigala: challenging the solar maximum in brazil with polarxs. *In: Proceeding of the ION GNSS 2011. Portland, Oregon*.

Chen, F. F. (2006). *Introduction to plasma physics and controlled fusion* (3rd ed.). New York, NY: Springer.

Crane, R. K. (1976). Spectra of ionospheric scintillation. *J. Geophys. Res.*.

Franke, S. J., Liu, C. H., & Fang, D. J. (1984). Multifrequency study of ionospheric scintillation at ascension island. *Radio Science*, *19*(3), 695–706.

Fremouw, E. (1980). Geometrical control of the ratio of intensity and phase scintillation indices. *Journal of Atmospheric and Terrestrial Physics*, *42*(9-10), 775-782. doi: 10.1016/0021-9169(80)90080-X

Haerendal, G. (1973). Theory of equatorial spread f. *Technical report, Munich, Germany: Max Planck Institute for Extraterrestrial Physics*.

Jayachandran, P. T., Hamza, A. M., Hosokawa, K., Shiojwara, K., Macdougall, J. W., & Pokhotelov, D. (2017). Gps amplitude and phase scintillation associated with polar cap auroral forms. *J. Atmos. Solar Terr. Phys.*, *164*, 185-191. doi: https://doi.org/10.1016/j.jastp.2017.08.030.

Jayachandran, P. T., Langley, R. B., MacDougall, J. W., Mushini, S. C., Pokhotelov, D., Hamza, A. M., … Milling, D. K. (2009). Canadian high arctic ionospheric network (chain). *Radio Science*, *44*, 1 - 10. doi: 10.1029/2008RS004046

Jin, Y., Moen, J. I., Spicher, A., Oksavik, K., Miloch, W. J., Clausen, L. B. N., . . . Saito, Y. (2019). Simultaneous rocket and scintillation observations of plasma irregularities associated with a reversed flow event in the cusp ionosphere. *Journal of Geophysical Research: Space Physics*, *124*, 7098–7111. doi: 10.1029/2019JA026942

Kintner, P. M., Ledvina, B., & de Paula, E. (2007, September). Gps and ionospheric scintillations. *Space Weather*, *5*(9), S09001. doi: 10.1029/2006SW000260

Labelle, J., & Kelley, M. C. (1986, May). The generation of kilometer scale irregularities in equatorial spread f. *Journal of Geophysical Research*, *91*(A5), 5504–5512. doi: 10.1029/JA091iA05p05504

Leith, C. E. (1971). Atmospheric predictability and two-dimensional turbulence. *Journal of Atmospheric Sciences*, *28*(1), 145.

Mezaoui, H., Hamza, A. M., & Jayachandran, P. T. (2014, October). Investigating high-latitude ionospheric turbulence using global positioning system data. *Geophysical Research Letters*, *41*(19), 6570–6576. doi: 10.1002/2014GL061331

Rino, C. L. (1979). A power law phase screen model for ionospheric scintillation: 1. weak scatter. *Radio Science*, *14*, 1135-1145. doi: https://doi.org/10.1029/RS014i006p01135

Rino, C. L., Tsunoda, R. T., Petriceks, J., Livingston, R. C., Kelley, M. C., & Baker, K. D. (1981). Simultaneous rocket-borne beacon and in situ measurements of equatorial spread f-intermediate wavelength results. *Journal of Geophysical Research*, *86*(A4), 2411–2420. doi: 10.1029/JA086iA04p02411

Rufenach, C. L. (1972). Power-law wavenumber spectrum deduced from ionospheric scintillation observations. *Space Physics*, *77*, 4761-4772. doi: https://doi.org/10.1029/JA077i025p04761

Song, K., Hamza, A. M., Jayachandran, P. T., Meziane, K., & Kashcheyev, A. (2023, July). *Spectral characteristics of phase fluctuations at high latitude.* (Manuscript submitted for publication)

Song, K., Meziane, K., Kashcheyev, A., & Jayachandran, P. T. (2021). Multifrequency observation of high latitude scintillation: A comparison with the phase screen model. *IEEE Transactions on Geoscience and Remote Sensing*, *60*, 1-9. doi: 10.1109/TGRS.2021.3113778

Spicher, A., Miloch, W. J., & Moen, J. I. (2014). Direct evidence of double-slope power spectra in the high-latitude ionospheric plasma. *Geophysical Research Letters*(14), 1406-1412. doi: doi.org/10.1002/2014GL059214

Van Dierendonck, A. J., Klobuchar, J., & Hua, Q. (1993). Ionospheric scintillation monitoring using commercial single frequency c/a code receivers. *at the Sixth International Technical Meeting (ION GPS-93)*, 22-24.

Wernik, A. W., Secan, J. A., & Fremouw, E. J. (2003). Ionospheric irregularities and scintillation. *Advances in Space Research*, *31*(4), 971–981. doi: 10.1016/S0273-1177(02)00795-0

Yeh, K. C., & Liu, C.-H. (1982, April). Radio wave scintillations in the ionosphere. *Proceedings of the IEEE*, *70*, 324–360. doi: 10.1109/PROC.1982.12313

Yu, J., Xu, D., Rino, C. L., & Morton, Y. T. (2018). A multifrequency gps signal strong equatorial ionospheric scintillation simulator: Algorithm performance and characterization. *Aerospace and Electronic Systems IEEE Transactions on*, *54*, 1947-1965.

Two-component phase scintillation spectra in the auroral region: Observations and Model

Hamza, A. M., K. Song, K. Meziane, P. T. Jayachandran

Physics Department, University of New Brunswick, Fredericton, New Brunswick, Canada

Key Points:

- Dual power-law spectra observed in phase scintillation in the auroral region.
- Refraction versus diffraction.
- Ionospheric irregularities and their connection to amplitude and phase scintillation.

Abstract

The random amplitude and phase fluctuations observed in trans-ionospheric radio signals are caused by the presence of electron density irregularities in the ionosphere. Ground-based measurements of radio wave signals provide information about the medium through which these signals propagate. The Canadian High Arctic Ionospheric Network (CHAIN) Global Position System (GPS) receivers record radio signals emitted by the GPS satellites, enabling the study of their spectral characteristics.This study presents examples of phase spectra with two power-law components. These components exhibit steeper spectral slopes at higher frequencies and shallower ones at lower frequencies. In most cases, the breaking frequency point is statistically larger than the frequency associated with the Fresnel scale under the Taylor hypothesis. To be more specific, we conducted a spectral characterization of sixty (60) events recorded by the CHAIN Churchill GPS receiver, which is located in the auroral oval. When fluctuations above the background level are only observed in the phase, the spectra tend to be systematically steeper. Conversely, the power increase in higher frequency fluctuations accompanying amplitude scintillation tends to result in shallower spectra. A basic yet powerful model of radio wave propagation through a turbulent ionosphere, characterized by a power law electron density spectrum, can help to explain the two power laws observed in the scintillation events presented in this study by identifying the role played by small-scale ionospheric irregularities in diffraction.

Plain Language Summary

This study discusses the impact electron density irregularities in the ionosphere have on radio wave propagation. Ground-based measurements of Global Navigation Satellite System (GNSS) signals provide insights into their spectral characteristics. The study presents examples of phase spectra with two power-law components, showing steeper slopes at higher frequencies and shallower ones at lower frequencies. Phase fluctuations tend to result in steeper spectra, while amplitude scintillations lead to shallower spectra. The study suggests a simple model of radio wave propagation through a turbulent ionosphere to explain these observations.

1 Introduction

Radio wave scintillation is a physical phenomenon, first discovered by radio astronomers (see Hey et al. 1947), and associated with the distortion of radio waves emitted by astronomical sources and propagating through conducting media. Ionospheric scintillation is a particular case of the more general phenomenon of radio scintillation attributed to the distortion of radio waves emitted by the Global Navigation Satellite System (GNSS) when propagating through a turbulent ionosphere (Kintner et al., 2007; Rino, 1979). The cause of these signal fluctuations is attributed to the presence of irregularities in the ionospheric electron density. These irregularities arise when free energy is available in the form of currents or large-scale pressure gradients to trigger instability mechanisms, such as the Farley-Buneman and Gradient-Drift instabilities, which in turn redistribute the energy in space and time (Aarons, 1997; Rino et al., 1981). The conventional theories suggest that when the linear threshold conditions are met the instabilities are triggered and waves will grow until quasi-linear and nonlinear effects will dissipate the currents and flatten the gradients to bring back the plasma to thermodynamic equilibrium. The return to equilibrium happens through the temporal and spatial redistribution of the free energy (see Francis F. Chen 2016), which in turn impose the observed power spectra.

Radio waves propagating through the structured ionosphere undergo scattering, and it is the characteristics of various scattering processes that allow us to extract some of the fundamental ionospheric properties. On the ground, ionospheric scintillations are observed using Global Positioning System (GPS) receivers, which record time series and display patterns that are largely determined by the spatial and temporal conditions of the ionospheric medium through which the radio signals propagate (Mezaoui et al., 2014; Jayachandran et al., 2017; Labelle & Kelley, 1986; Basu et al., 1990; Fremouw, 1980; Rufenach, 1972; Rino, 1979; Crane, 1976). The spectral analysis of scintillations is particularly valuable since it reveals some of the characteristics of these irregularities (Rino, 1979; Yeh & Liu, 1982; Wernik et al., 2003; Song et al., 2021). Many studies have been conducted to try and resolve the refractive effects from the diffractive ones (see McCaffrey and Jayachandran, 2019; Ghobadi et al., 2020; McCaffrey and Jayachandran, 2021; Conroy et al., 2022) without bringing the problem to a close. Part of the challenge is due to signal detrending, and many methods have been proposed in the literature (see Forte and Radicella, 2002; Mushini et al., 2012; Spogli et al., 2021). The lack of a basic physical model, which would clearly identify the refractive from the diffractive effects, needs to be remedied, and we propose to do so in the second part of this manuscript.

By analogy with fluid turbulence, in a turbulent three-dimensional (3D) plasma, the energy cascades, i.e. the redistribution of energy, from the large scales to the smaller scales (Haerendal, 1973). This cascade of energy leads to power law spectra that reflect the partitioning of power among the various scale lengths on time scales often dictated by the growth and decay of irregularities in the plasma. When a fluid is constrained to flow within horizontal planes with negligible horizontal divergence, it exhibits 2D behaviour. A key feature of two-dimensional turbulence is the preferential accumulation of energy at large scales, where the energy inverse-cascades from smaller to larger scales. However, the dissipation of enstrophy occurs at small scales, leading to an inertial spectral range where enstrophy is transferred from large to small scales (Chen, 2006).

Plasma density irregularities ranging from scales of 100 km to few meters (the ion gyroradius) are observed in the high latitude ionosphere (Aarons, 1997; Rino et al., 1981). Notably, Jin et al. (2019) conducted recent research that uncovered double slope power spectra in electron density, with clearly defined breaking scales spanning from 33 m to 330 m. The transition to a steeper power-law would occur at scale size irregularities shorter than 125 m (Basu et al., 1990). Additionally, Spicher et al. (2014) reported that the electron density measured by the ICI-2 sounding rocket in the high-latitude ionospheric F layer plasma exhibits double-slope power laws in regions of strong density gradients, which can be associated with polar cap enhanced density regions and their front or trailing edges in particular. These findings establish connections between the existing body of experimental evidence of fluid-like plasma turbulence in the ionosphere and the predictions of various fluid plasma models proposed to describe the dynamics of the turbulent ionosphere.

In the present work, we take advantage of the large body of literature about two-dimensional (2D) Navier-Stokes turbulence (Leith, 1971) to try and understand the signatures observed in the GNSS data by constructing a simple wave propagation model. The physical mechanisms leading to the dual-cascade of enstrophy and energy observed in two-dimensional fluid turbulence can help us understand the signatures in the radio signals recorded by ground-based GPS receivers at auroral latitudes. In section 2, we describe the data collection. In section 3, the data analysis is conducted and the results are presented. Finally, section 4 is dedicated to a simple wave-propagation model to explain the results of the analysis and shed some light on the power-laws observed.

2 Data Description

The Canadian High Arctic Ionospheric Network (CHAIN) is a distributed array of ground-based radio instruments located in the Canadian Arctic region. CHAIN is designed to take advantage of Canadian geographic vantage points for monitoring and studying the high latitude ionosphere (Jayachandran et al., 2009). CHAIN instruments are GNSS Ionospheric Scintillation and TEC Monitors (GISTM) and High Frequency (HF)

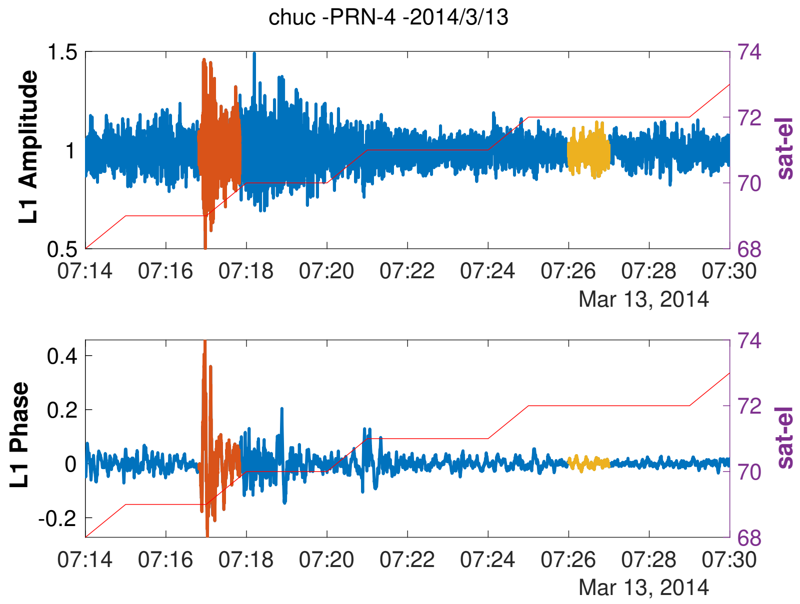

Figure 1. GPS L1 (1.575 GHz) measurements from 0714 to 0730 UTC for PRN4 at Churchill station (*chuc*) on Mar 13, 2014. While the top panel shows the signal amplitude, the bottom panel reports the carrier phase.

radars. The GISTMs in operation are Novatel GSV4004B and Septentrio PolaRxS Pro GNSS receivers (Van Dierendonck et al., 1993; Bougard et al., 2011). The Septentrio PolaRxS Pro is a multi-frequency, multi-constellation receiver, racking the L1, L2 and L5 signals independently of each other, and is designed for ionospheric studies and space weather applications. Each CHAIN receiver collects GPS observables from all visible GPS satellites. CHAIN has few locations with GISTM receivers recording data on L1, L2, and L5 frequencies at a 100 Hz sampling rate. For the present study, measurements collected at the Churchill (*chuc*) station (Geographic latitude 58.76 N, Geographic longitude 265.91E) provide data at 100 Hz sampling rate.

3 Results

For the present study, sixty-one scintillation events at the Churchill stations have been identified and selected during the time interval ranging from the year 2014 to 2021. A standard sixth-order Butterworth filter with a cutoff frequency of $f_c = 0.1$ Hz was used to detrend the amplitude and phase fluctuations. After obtaining the detrended signals, the amplitude and phase indices S_4 and σ_Φ are computed and used to identify scintillation events in the amplitude and phase, respectively. All scintillation events used in this analysis with scintillation indices S_4 and σ_ϕ are less than 0.1, which can be attributed to a weak scintillation regime. Once an event is selected, the spectral analysis of phase variations is carried out.

Figure 1 illustrates an example of phase and amplitude measurements collected at the *chuc* station for GPS PRN4, taken at a high elevation angle on March 13, 2014, from 0714 UT to 0730 UT. The top and bottom panels depict the detrended amplitude and phase at the L1 frequency, respectively. The right y-axis indicates the elevation angle in degrees. Our focus is on the time interval between 07:18:00 and 07:19:10 UT, highlighted by the red traces. During this interval (red trace), Figure 1 illustrates variations

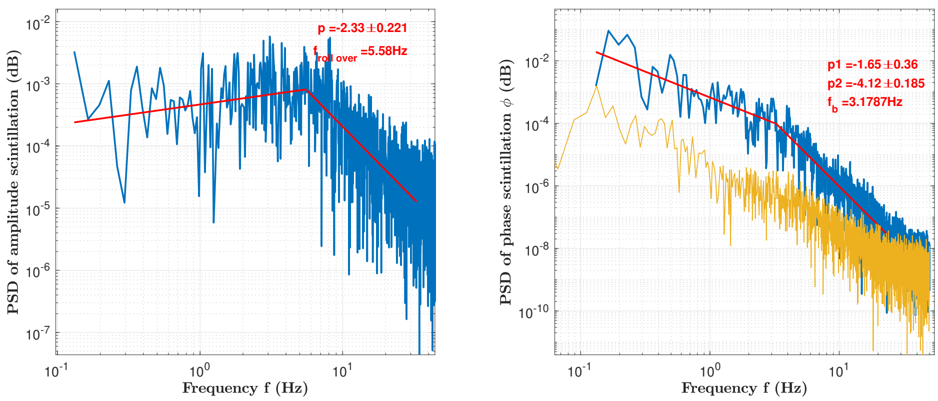

Figure 2. Left panel: amplitude scintillation spectrum. Right panel: Phase scintillation spectrum (blue) and the background noise spectrum is shown in yellow. On both panels, the best linear fit to fluctuations is indicated by the red straight line.

in carrier phase while observing minimal fluctuations in amplitude. Throughout the entire period of interest, both the signal amplitude and phase consistently remain elevated above the background level (yellow trace). We now proceed with the analysis by examining the spectral characteristics of the observed signal fluctuations. The spectral analysis of the phase and amplitude scintillation obtained for L1 is presented in Figure 2.

In Figure 2, the left panel provides the power density spectrum of amplitude scintillation. The right panel displays the phase scintillation spectrum (in blue) along with the background noise phase spectrum (in yellow). The red line represents the best fit for the measured spectrum. All spectra were obtained using the Fast Fourier Transform, with a time window of approximately 1 minute, and are presented in a log-log scale. Particularly, the amplitude scintillation spectrum exhibits a plateau below a critical frequency, denoted as f_0. This plateau suggests a region of relatively constant power density in the amplitude scintillation. The fit parameters for the amplitude spectrum include the spectral slope ($p = 2.33 \pm 0.22$) and the breaking frequency ($f_0 = 5.58$ Hz), which are labeled in the left panel of Figure 2. In contrast, the phase spectrum demonstrates two distinct components above the noise floor, in contrast to previously observed spectra with a single spectral slope. The noise spectrum (depicted in yellow) aids in visually identifying the noise frequency. A breakpoint frequency of $f_b = 3.9$ Hz is observed in the phase spectrum, indicating a transition between the two slopes. More precisely, the power density spectrum in Figure 2 reveals a distinct double-slope pattern for frequencies below approximately 11 Hz. Within this range, there are two distinct regions with different spectral slopes. The lower-frequency region, spanning from 0.1 Hz to 3.9 Hz, exhibits a relatively moderate slope of $p_1 = -1.79{\pm}0.245$. On the other hand, the higher-frequency region, ranging from 3.9 Hz to 11 Hz, displays a steeper slope of $p_1 = -4{\pm}0.236$. The precise values of the fit parameters and their corresponding errors are provided for each panel in Figure 2. The disparity in slope values between p_2 and p_1 is evident, indicating that the higher-frequency region exhibits a more pronounced and steeper change compared to the lower-frequency region. This finding is consistent with the study conducted by Spicher et al. (2014). Furthermore, when comparing the phase scintillation spectrum and the amplitude scintillation spectrum, clear differences can be observed. The amplitude scintillation spectrum displays a single slope above the critical frequency $f_0 = 5.58$ Hz, indicating a consistent spectral behavior. However, the phase scintillation spectrum exhibits a distinct double-slope pattern with a breakpoint frequency of $f_b = 3.9$ Hz. The

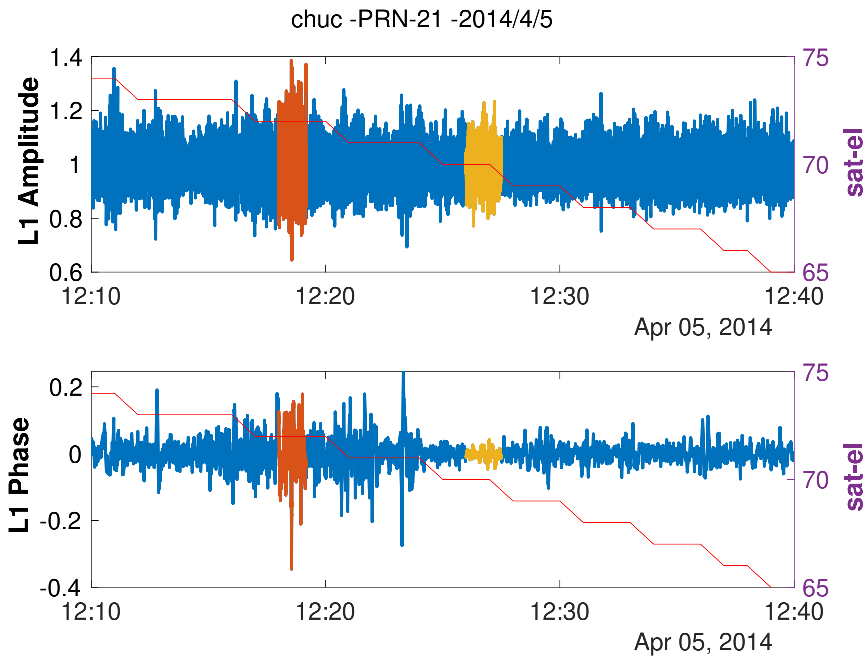

Figure 3. GPS L1 (1.575 GHz) measurements from 1210 to 1240 UTC for PRN21 at Churchill station (*chuc*) on April, 5, 2014. While the top panel shows the signal amplitude, the bottom panel depicts the carrier phase.

presence of two distinct components in the phase spectrum indicates that the spectral slopes differ from those observed in the amplitude spectrum. It is worth noting that the critical frequency f_0 in the amplitude scintillation spectrum is not equal to the break-point frequency f_b in the phase scintillation spectrum.

Figure 3 presents a second example that exhibits similar characteristics to the previously analyzed event. The top and bottom panels of Figure 3 display the recorded signal amplitude and phase measurements, respectively, obtained from the *chuc* station for GPS PRN21 at a high elevation angle on April 5, 2014, between 12:10 and 12:40 UT. During a specific time interval (12:18:30-12:19:30 UT), significant variations in both phase and amplitude were observed, indicating the onset of amplitude and phase scintillation (represented by the red trace). The yellow trace represents the background noise, which assists in determining the noise phase spectrum. Figure 4 illustrates the power density spectra of amplitude and phase scintillation obtained by applying the Fast Fourier Transform (FFT) to a 60-second time window. The left panel displays the amplitude scintillation spectrum, while the right panel shows the phase scintillation spectrum. In contrast to the amplitude spectrum, which exhibits a single slope characterized by $p = -2.26 \pm 0.17$, the phase spectrum demonstrates a double-slope profile. This indicates the presence of two distinct spectral ranges suggesting two different physical mechanisms at play. By performing linear fits, the slope values for each segment of the phase spectrum can be determined. The lower-frequency region, ranging from 0.1 Hz to 3.9 Hz, exhibits a relatively shallow slope of $p_1 = 1.79 \pm 0.245$, while the higher-frequency region, spanning from 3.9 Hz to 11 Hz, displays a steeper slope of $p_2 = 4 \pm 0.236$. Notably, the slope p_2 is found to be twice as big as p_1.

The same spectral analysis, as described above, was conducted for a total of sixty-one events collected between 2014 and 2021 at the *chuc* station. Figure 5 displays the

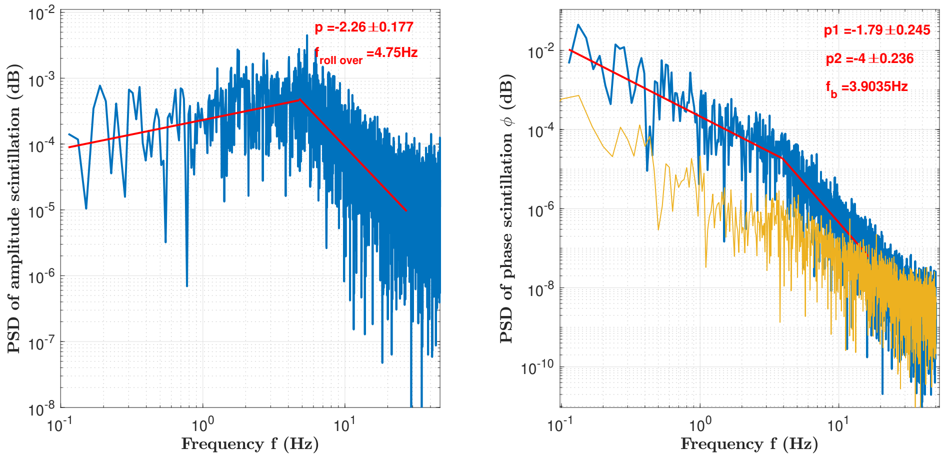

Figure 4. Same format as in Figure 2.

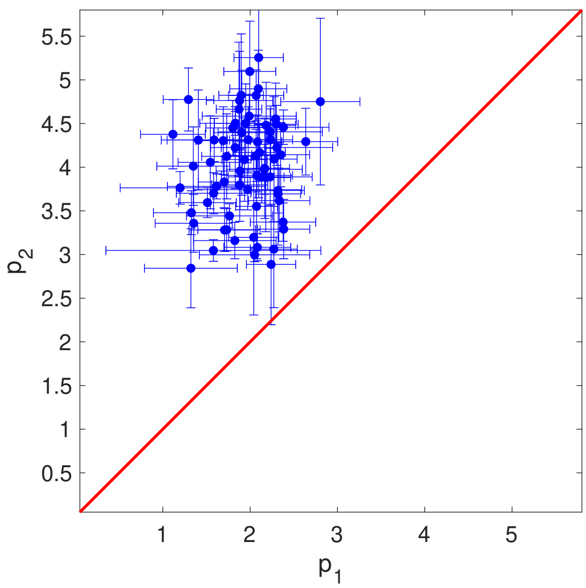

Figure 5. The p_2 values, representing the spectral power index of phase scintillation at higher frequencies (y-axis), are plotted against the corresponding p_1 values at lower frequencies (x-axis). The red straight line represents the line of slope unity.

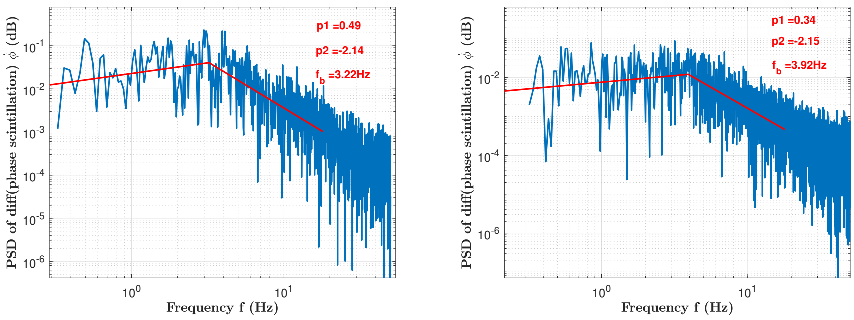

Figure 6.

results obtained from this analysis, comparing the spectral power index of phase scintillation at lower frequencies (y-axis) with the spectral power index at higher frequencies (x-axis). The error bars in the plot represent the uncertainty in the power index values, denoted by p. The red straight line in the plot represents the equality of spectral slope values between the two components of the phase scintillation spectral slopes p_1 and p_2. The results depicted in Figure 5 clearly demonstrate that, for all the scintillation events analyzed, the slope at higher frequencies is consistently steeper when compared to the slope at lower frequencies. This observation indicates that the high-frequency range of the phase scintillation spectrum exhibits a steeper spectral slope in comparison to the low-frequency portion.

In order to shed some light on the existence of two power-law spectra for the phase, we will compute the time-derivative of the phase and analyze its spectrum. When the Taylor hypothesis is satisfied, the time-derivative of the phase is directly related to the gradient of the phase, which represents the local component of the wave vector of the radio wave. if we denote by $\phi(\mathbf{x}, z, t)$ the phase of the propagating wave ($\mathbf{x} \equiv (x, y)$), the total time derivative of this phase is given by:

$$\frac{d\phi}{dt} = \frac{\partial \phi}{\partial t} + \mathbf{v}_d \cdot \nabla_\perp \phi + \frac{\partial \phi}{\partial z}\frac{\partial z}{\partial t}$$

where $\mathbf{v}_d$ represents a uniform drift velocity in the (x,y) plane (allowing the Taylor hypothesis to hold), and when we identify $\frac{\partial \phi}{\partial t} = -\omega$ and $\frac{\partial \phi}{\partial z} = k$ with the local frequency and the local z-component of the wave vector, k, we can clearly observe that the spectrum of the time-derivative of the phase depends very strongly on the gradient of the phase in the (x,y) plane as we shall demonstrate in section 4 below.

In the absence of small scale ionospheric electron density irregularities, the component of the phase-gradient along the direction of propagation is invariant and refraction is dominant. However, when small-scale electron density irregularities are present, diffraction takes over and large fluctuations in the phase-gradient along the direction of propagation arise as consequence. In other words, the time-derivative of the phase, when the Taylor hypothesis holds, represents this component of the phase-gradient, and its power spectrum should be directly related to the electron density power spectrum as will be discussed thoroughly in the section below describing an analytical model.

The phase derivative is obtained by differentiating the phase signal with respect to time and applying the Fourier Transform to obtain its spectrum. Figure 6 illustrates the phase derivative spectra for two scintillation events: the left panel corresponds to the event depicted in Figure 1, and the right panel corresponds to the event showcased in Figure 3. In Figure 6, it is clear that the phase derivative spectra display two distinct components with a breakpoint frequency, f_b, similar to the breakpoint frequency observed in Figure 2 and Figure 4, respectively. However, notable disparities in spectral slope values and overall shape are apparent when compared to the phase scintillation spectra depicted in the right panels of Figure 2 and Figure 4. Notably, the low-frequency region of the phase derivative spectrum appears flat, indicating minimal variations with a slope close to zero. Conversely, the high-frequency (corresponding to high wave numbers when the Taylor hypothesis holds) region of the spectrum aligns with the p_1 value observed in the right panels of Figure 2 and Figure 4, reflecting a steeper slope at small scales, large wave numbers. These findings provide valuable insights into the understanding of phase scintillation phenomena especially when it comes to separating the impacts of refraction from those of diffraction.

Table 1. Spectral slopes of derivative ($\dot{\phi}$ PSD) and Spectral slopes of phase scintillation (ϕ PSD)

Date of event	Spectral slope of $\dot{\phi}$ PSD		Spectral slope of ϕ PSD	
	p_1	p_2	p_1	p_2
2014/3/13	0.34	−2.1	−1.7	−3.9
2014/4/3	0.24	−1.8	−1.8	−3.3
2014/4/5	0.49	−2.1	−1.8	−4
2014/4/18	−0.08	−1.9	−2.1	−4.1
2014/4/20	0.10	−1.7	−1.8	−4.6
2014/4/28	0.20	−1.9	−1.7	−4.0
2014/10/26	−0.10	−2.0	−2.1	−4.0
2014/10/20	0.01	−1.7	−1.7	−4.7
2014/11/4	−0.09	−2.1	−2.1	−3.1
2018/9/10	0.11	−1.7	−1.6	−2.9
2017/9/8	−0.06	−1.8	−2.0	−3.8
2017/9/8	0.09	−1.7	−2.0	−3.2
2019/8/5	−0.02	−2.7	−2.6	−4.4
2021/5/12	−0.13	−2.2	−2.1	−3.6

Table 1 presents a summary of the double-spectral slopes for the phase derivative spectra and phase scintillation spectra. The first column of the table indicates the dates of the scintillation events. The second and third columns represent the spectral slopes, denoted as p_1, and p_2, respectively, in the phase derivative spectrum at the lower and higher frequency ranges. The fourth and fifth columns display the corresponding spectral slopes, p_1, and p_2, in the phase scintillation spectrum. It is clearly illustrated that the spectral slope of the phase derivative at lower frequencies tends towards zero. On the other hand, the spectral slope of the phase derivative at higher frequencies is similar to the spectral slope observed in the phase scintillation spectrum at lower frequencies. This observation suggests that the high-frequency portion of the phase derivative spectrum exhibits a slope comparable to the slope observed in the low-frequency portion of the phase scintillation spectrum.

4 A Radio Wave Propagation Model for the Dual Power Laws

Studies reported in the literature have suggested that Rayleigh-Taylor generated turbulence becomes anisotropic at intermediate and long wavelength (Bhattacharyya & Rastogi, 1986). Under such condition, there is no universal power law which describes the intermediate-scale irregularities(Franke et al., 1984).

As mentioned in Section 1, observational evidence for two-component irregularity power spectrum has been reported. Possible mechanisms giving rise to a break in the irregularity spectrum was discussed by (Bhattacharyya & Rastogi, 1986). It is evident that the presence of a break-point in the irregularity spectrum yields a two-component scintillation spectrum.

In our attempt to account for the two-component power law observed in the phase fluctuations, we have relied solely on the solution to the wave equation governing the propagation, which constitutes the backbone of the proposed model with no additional elements or hypothesis. From a fundamental point of view, the theoretical treatment of the propagation of an electromagnetic wave through a turbulent medium is a classical one, and might appear anachronistic given that it has attracted for many decades, and for various reasons, the interest of scientists and engineers.

In the ionospheric scintillation context, however, where refraction and diffraction are entangled, very few physical models are available to help underpin the pertinent factors that can fully capture the spectral features of the radio signal phase and amplitude fluctuations The simple model described below is an attempt to disentangle various scattering effects, and precisely addresses how the irregularity properties reflect on scintillation measurements on the ground. In particular, the model-framework presented in this section departs from some of the conventional standard formulation of scintillation models (Yu et al., 2018; Rino et al., 1981) by precisely identifying the role played by ionospheric irregularities in determining the type of scintillation event one should observe.

The fundamental equation describing the evolution of the electric and magnetic field components of an electromagnetic wave is given by:

$$\left\{\nabla^2 - \frac{\epsilon(\mathbf{x}, z, t)}{c^2}\frac{\partial^2}{\partial t^2}\right\}\delta E_j(\mathbf{x}, z, t) = 0 \tag{1}$$

where δE_j is any component of the electric field, $\epsilon(\mathbf{x}, z, t)$ the medium dielectric function and c the speed of light in the vacuum. Further down the derivation, the j-index is omitted. The index of refraction is defined by:

$$n(\mathbf{x}, z, t) = \sqrt{\epsilon(\mathbf{x}, z, t)} \tag{2}$$

where ψ is the Fourier transform of $\delta E(\mathbf{x}, z, t)$ in time, with

$$\delta E(\mathbf{x}, z, t) = \frac{1}{2\pi}\int e^{i(kz-\omega t)}\psi(\mathbf{x}, z, \omega)d\omega \tag{3}$$

Applying the Fourier transform to the wave equation (1) leads

$$2ik\frac{\partial\psi}{\partial z} + \nabla_\perp^2\psi + k^2(\epsilon - 1)\psi = -\frac{\partial^2\psi}{\partial z^2} \tag{4}$$

given the definition of the dielectric function in its most simple form

$$\epsilon - 1 = n^2 - 1 = -\frac{4\pi e^2}{m\omega^2}N(\mathbf{x}, z) \tag{5}$$

$$2ik\frac{\partial\psi}{\partial z} + \nabla_\perp^2\psi - r_e N(\mathbf{x}, z)\psi = -\frac{\partial^2\psi}{\partial z^2} \tag{6}$$

where $r_e = \frac{4\pi e^2}{mc^2} \approx 2.8 \times 10^{-15}m$ is the classical electron radius.

We neglect the right hand side of the final equation (4) (The second order derivative with respect to the direction of propagation z). This approximation is often encountered in the literature as the "quasi-optics" approximation or "parabolic" approximation. The absence of a second derivative with respect the "z" means no curvature in the z-direction, which physically translates to the absence of reflected waves in the z-direction. The wave equation becomes:

$$2ik\frac{\partial\psi}{\partial z} + \nabla_\perp^2\psi - r_e N(\mathbf{x}, z)\psi = 0 \tag{7}$$

A note, worthy of mention, is the fact this last equation is the analog of the two-dimensional time-dependent Schrodinger equation, with time replaced by the spatial coordinate z, and the time dependent potential represented by the z-dependent electron density. There is a trivial invariant for the Schrodinger equation:

$$I = \int d\mathbf{x}|\psi(\mathbf{x}, z)|^2 = \int d\mathbf{x}|\psi(\mathbf{x}, 0)|^2 \tag{8}$$

The energy-like function $T(z)$ is not invariant.

$$T(z) = \int d\mathbf{x}\left[\frac{1}{2k}(\nabla_\perp\psi)^2 + \frac{r_e}{2k}N(\mathbf{x}, z)|\psi(\mathbf{x}, z)|^2\right] \tag{9}$$

with

$$\frac{dT(z)}{dz} = \frac{r_e}{2k}\int d\mathbf{x}\frac{\partial N(\mathbf{x}, z)}{\partial z}|\psi(\mathbf{x}, z)|^2 \tag{10}$$

The analog for energy $E(z)$ can be considered an adiabatic invariant when the dependence of the electron density on z is weak.

We now introduce the eikonal approximation and write $\psi(\mathbf{x}, z)$ as:

$$\psi(\mathbf{x}, z) = A(\mathbf{x}, z)\exp iS(\mathbf{x}, z) \tag{11}$$

where $A(\mathbf{x}, z)$ and $S(\mathbf{x}, z)$ are real functions. Note that we need to keep track of the fact that the total phase includes the term $e^{i(kz-\omega t)}$, which leads to a total phase $\phi(\mathbf{x}, z, t) = S(\mathbf{x}, z) + kz - \omega t$, and which suggests a slow z-dependence of $S(\mathbf{x}, z)$. We should point out the fact that the gradient and time derivative of the total phase define the local wave number and the local frequency as follows:

$$\begin{aligned} \frac{\partial\phi}{\partial z} &= \frac{\partial S}{\partial z} + k \\ \nabla_\perp\phi &= \nabla_\perp S \\ \frac{\partial\phi}{\partial t} &= -\omega \end{aligned} \tag{12}$$

We insert the expression for ψ (11) into the wave equation (7), which leads to a system of coupled equations describing the evolution of the amplitude and phase of the wave, respectively.

$$\frac{\partial S}{\partial z} - \frac{1}{2k}\frac{\nabla_\perp^2 A}{A} + \frac{1}{2k}(\nabla_\perp S)^2 + \frac{r_e}{2k}N = 0 \tag{13}$$

$$\frac{\partial A^2}{\partial z} + \nabla_\perp\cdot[\frac{A^2}{k}\nabla_\perp S] = 0 \tag{14}$$

Note that if we neglect the variations of the amplitude in the plane perpendicular to the direction of propagation z, we obtain the following set of equations:

$$\frac{\partial S}{\partial z} + \frac{1}{2k}(\nabla_\perp S)^2 + \frac{r_e}{2k}N = 0 \tag{15}$$

$$\frac{\partial A^2}{\partial z} + \frac{A^2}{k}\nabla_\perp^2 S = 0 \tag{16}$$

note that equation (16) can also be written in a more compact form as follows:

$$\frac{\partial\left[\ln A^2\right]}{\partial z}+\frac{1}{k}\nabla_\perp^2 S=0 \tag{17}$$

Equations (15) shows the phase is directly affected by the electron density and its fluctuations. The second term in equation (15), $(\nabla_\perp S)^2$, is the refractive term. Indeed, one can define the local wave vector by its components $(\nabla_\perp S, k+\frac{\partial S}{\partial z})$, which suggests that the component $\nabla_\perp S$ determines the amount of rotation away from the z-axis when $\frac{\partial S}{\partial z}$ is negligible, and is therefore linked to refraction. On the other hand, equation (16) shows that the amplitude is affected by the curvature of the phase, $\nabla_\perp^2 S=\nabla_\perp\cdot\nabla_\perp S$, which is a measure of steepest descent and identifies minima and maxima in the wave fronts, and is directly linked to diffraction. Note also that this Laplacian can be interpreted in terms of the divergence of the local perpendicular component of the wave-vector $\nabla_\perp S$. In other words, in the absence of small scale structures in the electron density, the amplitude does not change (see (Song et al., 2023)). We should also point out the fact that refraction can be quantified by the ratio $\frac{|\nabla_\perp S|}{k}$, while diffraction depends solely of the curvature of the phase S.

The invariants (adiabatic invariant included), introduced above, can be expressed in terms of the amplitude and phase as follows,

$$\begin{aligned}
I &= \int d\mathbf{x}A^2(\mathbf{x},z)=\int d\mathbf{x}A^2(\mathbf{x},0)\\
T &= \frac{1}{2k}\int d\mathbf{x}\left[(\nabla_\perp A)^2+(\nabla_\perp S)^2A^2+r_eNA^2\right]
\end{aligned} \tag{18}$$

Since we are primarily interested in power spectra, we will use the two-dimensional Fourier transforms of the Amplitude and the phase as defined by:

$$\begin{aligned}
A(\mathbf{x},z) &= \int d\mathbf{q}e^{i\mathbf{q}\cdot\mathbf{x}}A(\mathbf{q},z)\\
S(\mathbf{x},z) &= \int d\mathbf{q}e^{i\mathbf{q}\cdot\mathbf{x}}S(\mathbf{q},z)
\end{aligned} \tag{19}$$

which in turn leads to the following equations for the Fourier components of the amplitude and phase, respectively,

$$\begin{aligned}
S(\mathbf{q},z) &= -\frac{r_e}{2k}\int^z dz_1 N(\mathbf{q},z_1)\\
&+ \frac{k}{2}\int^z dz_1\int d\mathbf{p}\frac{\mathbf{p}\cdot(\mathbf{q}-\mathbf{p})}{k^2}S(\mathbf{p},z_1)S(\mathbf{q}-\mathbf{p},z_1)
\end{aligned} \tag{20}$$

$$\begin{aligned}
\left[\ln A^2\right](\mathbf{q},z) &= \frac{q^2}{k}\int^z dz_1 S(\mathbf{q},z_1)\\
&+ k\int^z dz_1\int d\mathbf{p}\frac{\mathbf{p}\cdot(\mathbf{q}-\mathbf{p})}{k^2}S(\mathbf{p},z_1)\left[\ln A^2\right](\mathbf{q}-\mathbf{p},z_1)
\end{aligned} \tag{21}$$

Note that if we follow the notation in (Yeh & Liu, 1982) and write $A(\mathbf{x},z)=e^{\chi(\mathbf{x},z)}$, then $\left[\ln A^2\right]=2\chi(\mathbf{x},z)$. It becomes clear that the second equation (21) is nothing but the equation for the Fourier transform of $\chi(\mathbf{x},z)$, which can be explicitly expressed as:

$$\chi(\mathbf{q},z)=\frac{q^2}{2k}\int^z dz_1 S(\mathbf{q},z_1)+k\int^z dz_1\int d\mathbf{p}\frac{\mathbf{p}\cdot(\mathbf{q}-\mathbf{p})}{k^2}S(\mathbf{p},z_1)\chi(\mathbf{q}-\mathbf{p},z_1) \tag{22}$$

in fact, one can easily show the equation governing the variation of the amplitude with height (z) can be cast in the following form:

$$\frac{\partial\chi}{\partial z}+\nabla_\perp\chi\cdot\frac{\nabla_\perp S}{k}+\frac{1}{2k}\nabla_\perp^2 S=0 \tag{23}$$

which, in the case when one can neglect the variation of the amplitude in the plane perpendicular to the direction of propagation or neglect the effects of refraction (second term in equation (23)), shows that the variation of the amplitude depends solely on the curvature of the phase. This clearly shows how diffraction affects the amplitude of the wave.

Note also that given the size of $r_e \approx 10^{-15}m$ and given the typical ionospheric densities of $N \approx 10^{11}m^{-3}$, the term $r_eN \approx 10^{-4}m^{-2}$.

From a dimensional analysis of equation (7), and introducing the Fresnel scale length $L_F = \sqrt{\lambda z} \approx 500$ m for the type of ionospheric problem we want to address, a perpendicular scale $L_\perp$ for the phase and a scale length L_c for the curvature of the phase, we can estimate from equations (15) and (16):

$$\left\{2k\frac{\partial S}{\partial z}\right\} \approx \frac{[S]}{L_F^2} \approx 4\times10^{-6}[S] \quad ; \quad \left\{(\nabla_\perp S)^2\right\} \approx \frac{[S]^2}{L_\perp^2} \quad ; \quad \{r_eN\} \approx 10^{-4}m^{-2} \tag{24}$$

$$\left\{k\frac{\partial\left[\ln A^2\right]}{\partial z}\right\} \approx \frac{\left[\ln A^2\right]}{L_F^2} \approx 4\times10^{-6}\left[\ln A^2\right] \quad ; \quad \left\{\nabla_\perp^2 S\right\} \approx \frac{[S]}{L_c^2} \tag{25}$$

comparing the size of these terms allows us to identify the dominant scattering mechanisms. In the absence of small scale structures in the density, and noting that the second term in equation (24) when dominant leads to the geometrical optics approximation and a mathematical description of refraction when balanced with the electron density term. On the other hand, when the electron density is structured and small scale structures arise with length scales comparable to the fresnel scale, diffraction kicks in, and the second term in equation (25) becomes large enough to affect the amplitude.

We will now focus on identifying the physical mechanism(s) responsible for the appearance of dominant power laws in the power spectrum for the phase of radio signals detected by GPS receivers located in the auroral zone. To accomplish this task, we turn to the invariants identified above and express them in terms of Fourier components of the amplitude and phase.

$$\begin{aligned} I &= \int d\mathbf{x}|\psi(\mathbf{x},z)|^2 = \int d\mathbf{x}|A(\mathbf{x},z)|^2 \\ &= \int d\mathbf{q}|A(\mathbf{q},z)|^2 = \int d\mathbf{q}|A(\mathbf{q},z=0)|^2 \end{aligned} \tag{26}$$

$$\begin{aligned} 2kT &= \int d\mathbf{q}q^2|A(\mathbf{q},z)|^2 \\ &+ r_e\int d\mathbf{q}N(\mathbf{q},z)\int d\mathbf{p}A(\mathbf{p},z)A^*(\mathbf{q}+\mathbf{p},z) \\ &+ \int d\mathbf{q}A(\mathbf{q},z)\int d\mathbf{p}\int d\mathbf{r}\left[\mathbf{r}\cdot(\mathbf{q}-\mathbf{p}-\mathbf{r})\right]A^*(\mathbf{p},z)S(\mathbf{r},z)S^*(\mathbf{q}-\mathbf{p}+\mathbf{r},z) \end{aligned} \tag{27}$$

Note that because $A(\mathbf{x},z)$ and $S(\mathbf{x},z)$ are real functions, the complex conjugates of their Fourier components satisfy $A^*(\mathbf{q},z) = A(-\mathbf{q},z)$ and $S^*(\mathbf{q},z) = S(-\mathbf{q},z)$. The first expression (26) is an absolute invariant while the second (27) is an adiabatic one as discussed above. Given the two expressions for the phase and the amplitude (20,21), there is clearly a closure problem. We shall iterate to only include terms to order r_e^2. The results are:

$$I = \int d\mathbf{q}|A(\mathbf{q},z=0)|^2 \tag{28}$$

$$\begin{aligned} 2kT &= \int d\mathbf{q}q^2|A(\mathbf{q},z)|^2 \\ &+ r_e\int d\mathbf{q}N(\mathbf{q},z)\int d\mathbf{p}A(\mathbf{p},z)A^*(\mathbf{q}+\mathbf{p},z) \\ &+ \frac{r_e^2}{4}\int d\mathbf{q}A(\mathbf{q},z)\int d\mathbf{p}\int d\mathbf{r}\left[\frac{\mathbf{r}\cdot(\mathbf{q}-\mathbf{p}-\mathbf{r})}{k^2}\right]A^*(\mathbf{p},z)\, * \end{aligned}$$

$$* \quad \int^z dz_1 \int^z dz_2 N(\mathbf{r}, z_1) N(-\mathbf{q} + \mathbf{p} - \mathbf{r}, z_2) \tag{29}$$

We will now show that by imposing a single power law spectrum for the amplitude consistent with the first invariant, the second invariant will reveal two power laws, one directly related to the amplitude and a second one related to the electron density spectrum.

Let us assume that the amplitude and density spectra are isotropic and are given by:

$$|A(\mathbf{q}, z)|^2 = C_A q^\alpha \quad for \quad q_{Ai} \le q \le q_{Ad} \tag{30}$$
$$|N(\mathbf{q}, z)|^2 = C_N q^\beta \quad for \quad q_{Ni} \le q \le q_{Nd} \tag{31}$$

where C_A, C_N are constants and where q_{Ai} and q_{Ad} are the limits of the amplitude spectrum. Similarly, q_{Ni} and q_{Nd} represent the limits of the electron density spectrum.

To order r_e, the two invariants are given by:

$$I = 2\pi C_A \int_{q_{Ai}}^{q_{Ad}} dq q^{\alpha+1} \tag{32}$$

$$\begin{aligned} T &= \frac{\pi C_A}{k} \int_{q_{Ai}}^{q_{Ad}} dq q^{\alpha+3} \\ &+ \frac{r_e}{2k} \int d\mathbf{q} N(\mathbf{q}, z) \int d\mathbf{p} A(\mathbf{p}, z) A(-\mathbf{q} - \mathbf{p}, z) \end{aligned} \tag{33}$$

Given the assumption of isotropy, we can insert the expressions for the Fourier components of the amplitude and the density to obtain the power spectrum for the phase from the energy-like invariant T.

$$T = \frac{\pi C_A}{k} \int dq \left[q^{\alpha+3} + 2\pi r_e C_N^{\frac{1}{2}} q^{\frac{\beta}{2}+1} \left(\int^q + \int_q \right) dp |\mathbf{q} + \mathbf{p}]|^{\frac{\alpha}{2}} p^{\frac{\alpha}{2}+1} \right] \tag{34}$$

let us expand the $|\mathbf{q} + \mathbf{p}|^{\frac{\alpha}{2}} = (q^2 + p^2 + 2\mathbf{q} \cdot \mathbf{p})^{\frac{\alpha}{4}}$ as follows:

$$|\mathbf{q} + \mathbf{p}]|^{\frac{\alpha}{2}} = \begin{cases} q^{\frac{\alpha}{2}} \left(1 + \frac{p^2}{q^2} + 2\frac{\mathbf{q} \cdot \mathbf{p}}{q^2} \right)^{\frac{\alpha}{4}} & \text{if } q > p \\ p^{\frac{\alpha}{2}} \left(1 + \frac{q^2}{p^2} + 2\frac{\mathbf{q} \cdot \mathbf{p}}{p^2} \right)^{\frac{\alpha}{4}} & \text{if } p > q \end{cases}$$

which leads to the following expression for E when keeping the leading terms only:

$$T = \frac{\pi C_A}{k} \int dq \left[q^{\alpha+3} + 2\pi r_e C_N^{\frac{1}{2}} q^{\frac{\beta}{2}+1} \left(q^{\frac{\alpha}{2}} \int_{p_0}^q p^{\frac{\alpha}{2}+1} dp + \int_q^{p_1} p^{\alpha+1} dp \right) \right] \tag{35}$$

which finally leads to:

$$\begin{aligned} T &= \frac{\pi C_A}{k} \int dq \left[q^{\alpha+3} + 2\pi r_e C_N^{\frac{1}{2}} q^{\frac{\beta}{2}+1} \left(\frac{\alpha q^{\alpha+2}}{(\alpha+2)(\alpha+4)} - \frac{2q^{\frac{\alpha}{2}} p_0^{\frac{\alpha}{2}+2}}{\alpha+4} + \frac{p_1^{\alpha+2}}{\alpha+2} \right) \right] \\ &= \int dq \mathcal{E}(q) \end{aligned} \tag{36}$$

From this expression, we deduce the energy-like power spectrum:

$$\begin{aligned} \mathcal{E}(q) &= \frac{\pi C_A}{k} q^{\alpha+3} \\ &+ \frac{2\pi^2 r_e}{k} C_A C_N^{\frac{1}{2}} q^{\frac{\beta}{2}+\alpha+3} * \\ &* \left(\frac{\alpha}{(\alpha+2)(\alpha+4)} - \frac{2}{\alpha+4} \left(\frac{p_0}{q} \right)^{\frac{\alpha}{2}+2} + \frac{1}{\alpha+2} \left(\frac{p_1}{q} \right)^{\alpha+2} \right) \end{aligned} \tag{37}$$

Note that $(p_0/q) < 1$ and $(p_1/q) > 1$, and that for $-4 < \alpha < -2$ the last two terms in expression (37) can be dropped. This in turn leads to two dominant and competing terms in the energy-like power spectrum, and it is clear that for large q (small scales), the second term, which contains the information about the density spectrum, defines a new power law:

$$\mathcal{E}(q) \approx \frac{\pi C_A}{k} q^{\alpha+3} + \frac{2\pi^2 \alpha r_e C_A C_N^{\frac{1}{2}}}{k(\alpha+2)(\alpha+4)} q^{\frac{\beta}{2}+\alpha+3} \tag{38}$$

We now need to connect the phase power spectrum to the energy-like power spectrum $E(q)$. We can easily show and derive from equation (13) the following equation:

$$\int d\mathbf{x} A^2(\mathbf{x}, z) \frac{\partial S(\mathbf{x}, z)}{\partial z} + T(z) = 0 \tag{39}$$

the function $T(z)$ is by definition positive (see equation (18)), and consequently the first term should be negative for equation (39) to hold. We therefore conclude that the z-derivative of the phase should be small and negative; indeed, this is consistent with equation (15). We have assumed that $T(z) = T(0)$ is an adiabatic invariant, and this in turn allows us to deduce that the first term in equation (39) is also independent of z in the adiabatic limit. We should note that to first order in r_e the power spectrum of $\frac{\partial S(\mathbf{q},z)}{\partial z} = \dot{S}(\mathbf{q}, z)$ is the same as the power spectrum for the electron density (see equation (15)) when neglecting refraction (neglecting the term $(\nabla_\perp S)^2$ in equation (15)). However, when small scale structures arise in the density, one can no longer neglect the refractive term in equation (15) and the diffractive term in the amplitude equation (16), giving rise to competing power laws at two different scale ranges; a scale-range with scales much larger than the Fresnel scale, where diffractive effects are negligible, and a scale-range with small scales of the order of the Fresnel scale or smaller, where diffractive effects become dominant.

Since we are also interested in the power spectrum of $\frac{\partial S(\mathbf{q},z)}{\partial z} = \dot{S}(\mathbf{q}, z)$, equation (39) can be expressed in Fourier space.

$$\int d\mathbf{q} \dot{S}(\mathbf{q}, z) \int d\mathbf{p} A(\mathbf{p}, z) A(-(\mathbf{p}+\mathbf{q}), z) + \int dq \mathcal{E}(q) = 0 \tag{40}$$

note that we have already encountered the integral over $\mathbf{p}$ in equation (34). We can apply the same arguments to try and estimate this integral to obtain:

$$\int dq \left[-|\dot{S}(\mathbf{q}, z)| \frac{2\pi\alpha}{(\alpha+2)(\alpha+4)} + \frac{1}{2k} + \frac{\pi \alpha r_e C_N^{\frac{1}{2}}}{k(\alpha+2)(\alpha+4)} q^{\frac{\beta}{2}} \right] q^{\alpha+3} = 0 \tag{41}$$

if we assume the power spectrum of $\dot{S}(\mathbf{q}, z)$ to follow a power law, we can link the power index of the power spectrum for $\dot{S}$ to the power indices for the amplitude and the density. Note, as discussed above, that to first order in r_e the power spectrum for $\dot{S}$ is the power spectrum of the density as also suggested by the term in square brackets in equation (41).

$$\int dq \left[q^{\alpha+3} |\dot{S}(\mathbf{q}, z)| \right] = \frac{(\alpha+2)(\alpha+4)}{4\pi^2 C_A \alpha} T(z) = \frac{(\alpha+2)(\alpha+4)}{4\pi^2 C_A \alpha} T(0) \tag{42}$$

Equations (41) and (42) can be used interchangeably to calculate the power-law index of $\dot{S}$ in terms of the power-law indices for the amplitude and the density.

4.1 Summary: The Refractive limit

In the refractive limit, the curvature of the phase can be neglected and the equations governing the evolution of the amplitude and the phase of the propagating radio wave reduce to:

$$\frac{\partial \chi}{\partial z} + \left(\frac{\nabla_\perp S}{k} \right) \cdot \nabla_\perp \chi \quad \approx \quad 0$$

$$\frac{\partial S}{\partial z} + \frac{k}{2}\left(\frac{\nabla_\perp S}{k}\right)^2 + \frac{r_e}{2k}N \quad = \quad 0 \tag{43}$$

The ray-path is defined by

$$\frac{d\mathbf{x}}{dz} = \frac{\nabla_\perp S}{k}$$

which in turn leads to writing the equation for the amplitude as:

$$\frac{\partial \chi}{\partial z}dz + \nabla_\perp \chi \cdot d\mathbf{x} = d\chi \approx 0$$

which means that the amplitude does not change and the amplitude spectrum is invariant, which is consistent with the invariant analysis discussed above. The equation for the phase suggests that for small-angle refraction the phase is determined by the total electron content, which in this case is dominated by large scale electron density structures (small wave numbers). The refractive term in the equation for the phase (43) is quadratic and can be neglected for small-angle refraction, which leaves a phase completely dependent on the total electron content, and therefore a phase spectrum with very little power at large wave numbers.

4.2 Summary: The Diffractive Limit

In the diffractive limit, the gradient of the phase terms are neglected and the following set of governing equations is obtained:

$$\begin{aligned}
\frac{\partial \chi}{\partial z} + \frac{1}{2k}\nabla_\perp^2 S \quad &\approx \quad 0 \\
\frac{\partial S}{\partial z} + \frac{r_e}{2k}N \quad &\approx \quad 0
\end{aligned} \tag{44}$$

This set of equations can also be written in the following form:

$$S(\mathbf{x}, z) \quad \approx \quad -\frac{r_e}{2k}\int^z N(\mathbf{x}, z_1)dz_1 \tag{45}$$

$$S(\mathbf{q}, z) \quad \approx \quad -\frac{r_e}{2k}\int^z N(\mathbf{q}, z_1)dz_1$$

$$\begin{aligned}
\frac{\partial^2 \chi(\mathbf{x}, z)}{\partial z^2} \quad &\approx \quad \frac{r_e}{4k^2}\nabla_\perp^2 N(\mathbf{x}, z) \\
\chi(\mathbf{x}, z) \quad &\approx \quad \frac{r_e}{4k^2}\nabla_\perp^2 \int^z dz_1 \int^{z_1} N(\mathbf{x}, z_2)dz_2 \qquad (46) \\
\chi(\mathbf{q}, z) \quad &\approx \quad -\frac{r_e}{4k^2}q^2 \int^z dz_1 \int^{z_1} N(\mathbf{q}, z_2)dz_2
\end{aligned}$$

equations (45) and (46) show explicitly how the phase and amplitude are related to the density and the total electron content, respectively, and how the power spectra at large wave numbers, when small scale density structures are present, are related to the density spectrum.

5 Discussion and Conclusion

The model presented above is a simple model yet powerful enough to predict spectra with two power-laws. It also sheds some light on the method to adopt to resolve the difference between refractive and diffractive effects. Equations (15) and (16) constitute the backbone of the model with terms easily identifiable with refraction, $(\nabla_\perp S)^2$, with diffraction, $\nabla_\perp^2 S$, and with the electron density N and therefore with the total electron content when integration over z is performed. When small scale density irregularities are absent and refraction is dominant, the amplitude remains invariant throughout propagation and the amplitude power-law spectrum is also invariant. However, when small scale irregularities are present, the curvature of the phase is no longer negligible, and the contribution of the diffractive term to the amplitude equation suggest a readjustment of the power law. Moreover, the invariant I (related to the Born rule in quantum mechanics) suggests a shallower amplitude power law, which reflects the redistribution of power to small scale, large q. On the other hand, the presence of small scales in the density leads to a phase power spectrum similar to the density power spectrum.

6 Open Research

Data Availability Statement CHAIN data are available through `http://www.chain-project.net/data/gps/data/raw/`

7 Acknowledgements

Infrastructure funding for CHAIN was provided by the Canada Foundation for Innovation (CFI) and the New Brunswick Innovation Foundation (NBIF). CHAIN is maintained in collaboration with the Canadian Space Agency (CSA). This research was undertaken with the financial support of the Canadian Space Agency FAST program and the Natural Sciences and Engineering Research Council of Canada. Part of the funding for this research is provided by the Natural Sciences and Engineering Research Council Canada (NSERC).

References

Aarons, J. (1997, August). Global positioning system phase fluctuations at auroral latitudes. *Journal of Geophysical Research: Space Physics*, *102*, 17219–17231. doi: 10.1029/97JA01118

Basu, S., Basu, S., MacKenzie, E., Coley, W. R., Sharber, J. R., & Hoegy, W. R. (1990). Plasma structuring by the gradient drift instability at high latitudes and comparison with velocity shear driven processes. *Journal of Geophysical Research: Space Physics*, *95*, 7799–7818. doi: 10.1029/JA095iA06p07799

Bhattacharyya, A., & Rastogi, R. G. (1986). Phase scintillations due to equatorial F region irregularities with two-component power law spectrum. *Journal of Geophysical Research*, *91*(A10).

Bougard, B., Sleewaegen, J. M., Spogli, L., & Sreeja, J. F., V. V. Galera Monico. (2011). Cigala: challenging the solar maximum in brazil with polarxs. *In: Proceeding of the ION GNSS 2011. Portland, Oregon*.

Chen, F. F. (2006). *Introduction to plasma physics and controlled fusion* (3rd ed.). New York, NY: Springer.

Crane, R. K. (1976). Spectra of ionospheric scintillation. *J. Geophys. Res.*.

Franke, S. J., Liu, C. H., & Fang, D. J. (1984). Multifrequency study of ionospheric scintillation at ascension island. *Radio Science*, *19*(3), 695–706.

Fremouw, E. (1980). Geometrical control of the ratio of intensity and phase scintillation indices. *Journal of Atmospheric and Terrestrial Physics*, *42*(9-10), 775-782. doi: 10.1016/0021-9169(80)90080-X

Haerendal, G. (1973). Theory of equatorial spread f. *Technical report, Munich, Germany: Max Planck Institute for Extraterrestrial Physics*.

Jayachandran, P. T., Hamza, A. M., Hosokawa, K., Shiojwara, K., Macdougall, J. W., & Pokhotelov, D. (2017). Gps amplitude and phase scintillation associated with polar cap auroral forms. *J. Atmos. Solar Terr. Phys.*, *164*, 185-191. doi: https://doi.org/10.1016/j.jastp.2017.08.030.

Jayachandran, P. T., Langley, R. B., MacDougall, J. W., Mushini, S. C., Pokhotelov, D., Hamza, A. M., ... Milling, D. K. (2009). Canadian high arctic ionospheric network (chain). *Radio Science*, *44*, 1 - 10. doi: 10.1029/2008RS004046

Jin, Y., Moen, J. I., Spicher, A., Oksavik, K., Miloch, W. J., Clausen, L. B. N., ... Saito, Y. (2019). Simultaneous rocket and scintillation observations of plasma irregularities associated with a reversed flow event in the cusp ionosphere. *Journal of Geophysical Research: Space Physics*, *124*, 7098–7111. doi: 10.1029/2019JA026942

Kintner, P. M., Ledvina, B., & de Paula, E. (2007, September). Gps and ionospheric scintillations. *Space Weather*, *5*(9), S09001. doi: 10.1029/2006SW000260

Labelle, J., & Kelley, M. C. (1986, May). The generation of kilometer scale irregularities in equatorial spread f. *Journal of Geophysical Research*, *91*(A5), 5504–5512. doi: 10.1029/JA091iA05p05504

Leith, C. E. (1971). Atmospheric predictability and two-dimensional turbulence. *Journal of Atmospheric Sciences*, *28*(1), 145.

Mezaoui, H., Hamza, A. M., & Jayachandran, P. T. (2014, October). Investigating high-latitude ionospheric turbulence using global positioning system data. *Geophysical Research Letters*, *41*(19), 6570–6576. doi: 10.1002/2014GL061331

Rino, C. L. (1979). A power law phase screen model for ionospheric scintillation: 1. weak scatter. *Radio Science*, *14*, 1135-1145. doi: https://doi.org/10.1029/RS014i006p01135

Rino, C. L., Tsunoda, R. T., Petriceks, J., Livingston, R. C., Kelley, M. C., & Baker, K. D. (1981). Simultaneous rocket-borne beacon and in situ measurements of equatorial spread f-intermediate wavelength results. *Journal of Geophysical Research*, *86*(A4), 2411–2420. doi: 10.1029/JA086iA04p02411

Rufenach, C. L. (1972). Power-law wavenumber spectrum deduced from ionospheric scintillation observations. *Space Physics*, *77*, 4761-4772. doi: https://doi.org/10.1029/JA077i025p04761

Song, K., Hamza, A. M., Jayachandran, P. T., Meziane, K., & Kashcheyev, A. (2023, July). *Spectral characteristics of phase fluctuations at high latitude.* (Manuscript submitted for publication)

Song, K., Meziane, K., Kashcheyev, A., & Jayachandran, P. T. (2021). Multifrequency observation of high latitude scintillation: A comparison with the phase screen model. *IEEE Transactions on Geoscience and Remote Sensing*, *60*, 1-9. doi: 10.1109/TGRS.2021.3113778

Spicher, A., Miloch, W. J., & Moen, J. I. (2014). Direct evidence of double-slope power spectra in the high-latitude ionospheric plasma. *Geophysical Research Letters*(14), 1406-1412. doi: doi.org/10.1002/2014GL059214

Van Dierendonck, A. J., Klobuchar, J., & Hua, Q. (1993). Ionospheric scintillation monitoring using commercial single frequency c/a code receivers. *at the Sixth International Technical Meeting (ION GPS-93)*, 22-24.

Wernik, A. W., Secan, J. A., & Fremouw, E. J. (2003). Ionospheric irregularities and scintillation. *Advances in Space Research*, *31*(4), 971–981. doi: 10.1016/S0273-1177(02)00795-0

Yeh, K. C., & Liu, C.-H. (1982, April). Radio wave scintillations in the ionosphere. *Proceedings of the IEEE*, *70*, 324–360. doi: 10.1109/PROC.1982.12313

Yu, J., Xu, D., Rino, C. L., & Morton, Y. T. (2018). A multifrequency gps signal strong equatorial ionospheric scintillation simulator: Algorithm performance and characterization. *Aerospace and Electronic Systems IEEE Transactions on*, *54*, 1947-1965.